Monthly Notices
of the
ROYAL ASTRONOMICAL SOCIETY

MNRAS **457,** 4218–4235 (2016)
Advance Access publication 2016 February 9

doi:10.1093/mnras/stw264

Mass transfer between debris discs during close stellar encounters

Lucie Jílková,[1]★ Adrian S. Hamers,[1] Michael Hammer[2,3] and Simon Portegies Zwart[1]

[1]*Leiden Observatory, Niels Bohrweg 2, Leiden, NL-2333 CA, the Netherlands*
[2]*Cornell University, 614 Space Sciences Building, Ithaca, NY 14853, USA*
[3]*Department of Astronomy , Steward Observatory, University of Arizona, Tucson, AZ 85721, USA*

Accepted 2016 January 29. Received 2016 January 21; in original form 2015 November 17

ABSTRACT

We study mass transfers between debris discs during stellar encounters. We carried out numerical simulations of close flybys of two stars, one of which has a disc of planetesimals represented by test particles. We explored the parameter space of the encounters, varying the mass ratio of the two stars, their pericentre and eccentricity of the encounter, and its geometry. We find that particles are transferred to the other star from a restricted radial range in the disc and the limiting radii of this transfer region depend on the parameters of the encounter. We derive an approximate analytic description of the inner radius of the region. The efficiency of the mass transfer generally decreases with increasing encounter pericentre and increasing mass of the star initially possessing the disc. Depending on the parameters of the encounter, the transfer particles have a specific distribution in the space of orbital elements (semimajor axis, eccentricity, inclination, and argument of pericentre) around their new host star. The population of the transferred particles can be used to constrain the encounter through which it was delivered. We expect that many stars experienced transfer among their debris discs and planetary systems in their birth environment. This mechanism presents a formation channel for objects on wide orbits of arbitrary inclinations, typically having high eccentricity but possibly also close to circular (eccentricities of about 0.1). Depending on the geometry, such orbital elements can be distinct from those of the objects formed around the star.

Key words: planets and satellites: formation – circumstellar matter – planetary systems – open clusters and associations: general.

1 INTRODUCTION

Stars form in giant molecular clouds and in most cases, a group containing 10–10^4 stars form at a similar time from the same cloud (Lada & Lada 2003). Depending on the number of stars and their spatial and velocity distributions, these groups, with stellar densities relatively high compared to those of the field stars, are classified as stellar associations or star clusters (e.g. Bressert et al. 2010; Gieles & Portegies Zwart 2011). The gravitational interactions in these crowded environments result in close stellar encounters (for example, Binney & Tremaine 1987; Bonnell et al. 2001; Olczak, Pfalzner & Spurzem 2006; Pfalzner, Olczak & Eckart 2006; Olczak, Pfalzner & Eckart 2008; Olczak et al. 2012) that can strongly influence the properties of protoplanetary discs around the still young stars, and eventually the planetary systems formed from these (Clarke & Pringle 1993; Ostriker 1994). Several authors presented *N*-body simulations of planetary systems (for example, Hurley & Shara 2002; Spurzem et al. 2009; Parker & Quanz 2012; Zheng, Kouwenhoven & Wang 2015) and hydro-dynamical simulations of protoplanetary discs in star clusters (Rosotti et al. 2014; Muñoz et al. 2015). These works confirmed the importance of the star clusters and close stellar encounters for the dynamics of planetary systems and circumstellar discs. The rate and parameters of the encounters depend on the characteristics of the star cluster, such as its mass, density, initial spatial and velocity distributions (for example, Binney & Tremaine 1987; Bonnell et al. 2001; Adams et al. 2006; Malmberg et al. 2007; Olczak, Pfalzner & Eckart 2010; Craig & Krumholz 2013). Using *N*-body simulations, Craig & Krumholz (2013) tabulated the number and properties of encounters as a function of the cluster characteristics. For example, they measured the encounter rate (counting flybys closer than 1000 AU) for a solar-like star (0.8–1.2 $M_\odot$) of $\sim 1.9 \times 10^{-6}$ yr^{-1} experienced in a cluster with mass of 1000 $M_\odot$, typical radius of about 2.5 pc, virial ratio of 0.75, and a moderate degree of substructure (fractal dimension $D = 2.2$).

After stars form, gas and dust are present in their circumstellar discs, where planets and debris form later. The current knowledge of the debris discs has been summarized by Matthews et al. (2014), Krivov (2010) and Wyatt (2008). Debris discs are result of planet formation around main sequence stars and they consist of dust and large bodies (such as comets, asteroids, or planetesimals) which

★ E-mail: jilkova@strw.leidenuniv.nl

determine the dynamics of the discs. The dust grains are heated by the central star and they re-radiate in the infrared (IR), producing so-called IR excess in the spectral energy distribution of their host star, or (sub)millimeter wavelengths. It is the radiation of the dust that is observed. The dust has relatively short lifetime and is constantly replenished by collisions between the larger bodies (for example, Wyatt & Dent 2002). Debris discs have been observed around hundreds of stars. The detection rates vary depending on the wavelength, stellar type and age, and the relative sensitivity of the surveys (see Matthews et al. 2014, for the summary and references). Cold dust (at $\geq 60\,\mu$m) has been detected around 24 ± 5 and 32 ± 5 per cent of A stars (Thureau et al. 2014 at 100 μm and Su et al. 2006 at 70 μm, respectively) and around 20 ± 2 per cent of solar-type FGK stars (Eiroa et al. 2013). Dust in the mid-IR wavelengths ($\leq$60 μm) was detected around ∼11 per cent of solar-type stars (Dodson-Robinson et al. 2011).

The debris discs are observed to decay with time, as the planetesimals are depleted by collisions which grind them into dust (Dominik & Decin 2003). The planetesimals in debris discs must be stirred so that their relative velocities are sufficient for grinding. The origin of the stirring is still under discussion and several mechanisms have been suggested (Matthews et al. 2014): pre-stirring as a result of the protoplanetary phase (see Wyatt 2008, and references therein); stirring by planets in the same system (Kenyon & Bromley 2004a, Mustill & Wyatt 2009); self-stirring by sufficiently massive planetesimals (for example, Kenyon & Bromley 2008; Kennedy & Wyatt 2010, and references therein); or stirring by external process, such as stellar flybys (Kenyon & Bromley 2002).

1.1 Simulations of discs during stellar encounters

In the early gas-rich stages, the viscosity and pressure of the gas in a circumstellar disc are important for the general disc dynamics when considering the effects of external perturbers and close stellar encounters. For the more distant ones, where the periastron is larger than the size of the disc, gas and dust free simulations are commonly used to study the perturbations due the encounter and the debris disc is often modelled by test particles (Clarke & Pringle 1993 were among the first to use this approach, while they considered dissipation in the disc through pseudo-viscosity; discussion on the role of self-gravity, pressure and viscosity of the disc was carried for example by Pfalzner, Umbreit & Henning 2005b).

The dynamics of a planetesimal during a stellar encounter can be approximately described as a general restricted three-body problem. The planetesimals are much less massive than the two stars and their gravitational influence – mutual as well as on the stars – can be neglected. Planetesimals are then represented as (zero-mass) test particles that live in the time-dependent gravitational potential of the two stars that move on a conic section orbit. A similar approach was used already in the seminal work of Toomre & Toomre (1972), who pioneered the simulations of mergers of disc galaxies. The particles of the disc are perturbed during the encounter and can, in general, stay bound to their parent star, become bound to the perturbing star, or become unbound from the system. Previous work showed that depending on the parameters of the encounter and the initial size of the disc, the fate of the particles depends on their initial location in the disc around the parent star. For example, Clarke & Pringle (1993) noticed that in the prograde coplanar parabolic encounter of equal mass stars, all the particles located closer than ∼0.3 of the pericentre of the encounter to the parent star stay bound. Kobayashi & Ida (2001) confirmed this result and gave a more detailed description of the perturbation in eccentricity and semimajor axis of the disc particle orbits. A natural result of the encounter is a truncation of the disc and the dependence of the resulting disc size on the mass ratio between the encountering stars was recently described in detail by Breslau et al. (2014). The encounter can also induce various structures in the disc, such as rings or spiral patterns, or cause the disc to have an elliptical shape (Larwood & Kalas 2001; Pfalzner 2003). Simulations of the influence of a stellar flyby on a debris disc were also motivated to explain individual observed systems, for example, in case of β Pictoris by Larwood & Kalas (2001) and HD 141569 by Reche, Beust & Augereau (2009), or to understand the scattered Kuiper belt in the Solar system (e.g. Kobayashi, Ida & Tanaka 2005; Melita, Larwood & Williams 2005; Punzo, Capuzzo-Dolcetta & Portegies Zwart 2014). Results on the change of the disc mass or size due to the flybys were often applied in the simulations of star clusters, where the encounters occur (for example, Olczak, Pfalzner & Spurzem 2006; Pfalzner, Olczak & Eckart 2006; Lestrade et al. 2011; Vincke, Breslau & Pfalzner 2015; Portegies Zwart 2016).

1.2 Previous studies of captured planetesimals

Most of the studies that model a debris disc during stellar encounters focused on the evolution of the disc itself (its mass-loss, change of its size, morphology, energy or angular momentum). Depending on the parameters of the encounter, a portion of the disc can also be transferred from the parent star to the perturber. However a systematic study of the mass transfer among debris discs during a stellar flyby is still missing. As we describe below, captured bodies present an important output of stellar encounters and material originating from other stars might be present in many debris discs – including in the Solar system.

Clarke & Pringle (1993) investigated the response of an accretion disc to a stellar flyby. They represented the disc by test particles with pseudo-viscosity and carried out simulations of parabolic encounters of equal mass stars considering different initial geometries of the encounter orbit and the disc – coplanar prograde and retrograde, and orthogonal. They found that out of these three configurations, the mass transfer occurs only in the coplanar prograde encounter and that only the particles located initially $\gtrsim$0.35 of the pericentre distance from the parent star can be captured by the star initially without disc. These results were further extended by Hall, Clarke & Pringle (1996) who focused on energy and angular momentum exchanged during the encounter. They considered a more extended disc, up to four times the pericentre distance, and showed that particles are transferred from larger initial radii (beyond the pericentre distance) also in configurations when the disc is inclined with respect to the orbital plane (inclinations of 45°, 90°, 135° and 180°, where the latter corresponds to the coplanar retrograde encounter).

Larwood & Kalas (2001) studied prograde coplanar encounters and geometries with inclinations of the encounter orbit with respect to the disc of 30° and 60°. They varied the eccentricity of the encounter and found that planetesimals can be captured for eccentricities $\leq$2 while none are captured for eccentricities $\geq$5. The transferred material appeared to form an asymmetrical disc around their new host and showed clustering in eccentricities and semimajor axes.

From their parameter space study of stellar encounters, Pfalzner et al. (2005a) concluded that the mass transfer occurs nearly exclusively in prograde encounters. They investigated the dependence of the relative mass captured during prograde parabolic encounters on the mass ratio of the stars and the pericentre of the encounter. They found that the captured mass increases with the stellar mass ratio,

up to value of about 0.8 when the captured mass becomes almost independent of the stellar masses (they measured the mass ratio as the mass of the star initially without disc relative to the one initially with disc). They concluded that this might indicate the existence of an upper limit to the mass transfer for a given pericentre distance. They also found that the captured mass decreases almost linearly with increasing pericentre of the encounter.

Pfalzner et al. (2005b) presented the most detailed study of the mass transfers among circumstellar discs. They compared captures in parabolic and hyperbolic stellar orbits and confirmed that the transfer is smaller in the latter case (negligible for periastron larger than three times the disc size). They also found that the majority of the captured mass moves on highly eccentric orbits – in the equal mass parabolic encounter about 80 per cent of the particles have eccentricities above 0.8 and almost none below 0.4.

Planetesimals transferred during a stellar encounter were also suggested to explain the origin of some Solar system planetesimals in peculiar orbits (Kenyon & Bromley 2004b; Morbidelli & Levison 2004; Levison et al. 2010, 2010). The formation of the population of a so-called inner Oort cloud – which includes objects with pericentre $\gtrsim$50 AU and semimajor axis in range of 150–1500 AU (Trujillo & Sheppard 2014) – is still not well understood, because these orbits are too far away from the Sun to be influenced by planetary perturbations and too close to be substantially perturbed by the Galactic potential and encounters with the field stars (Portegies Zwart & Jílková 2015). Jílková et al. (2015) constrained the parameter space of encounters that could result in a population of planetesimals transferred to the Solar system that is consistent with the observed orbits of Sedna-like objects (Brown, Trujillo & Rabinowitz 2004; Trujillo & Sheppard 2014). Constraining the encounter is possible due to specific characteristics of the captured orbits.

Here we present a systematic study of the mass captured from a debris disc during a stellar encounter. We carried out simulations (Section 2) and measured how much material is transferred depending on the parameters of the encounter and what are the orbital characteristics of the particles before and after the transfer (Section 3). We derive an analytic approximation for the minimal radial distance of the particles to be captured by the encountering star and compare it with the results from the simulations (Section 4). We summarize and conclude in Section 5.

2 SIMULATIONS

We carried out simulations of stellar encounters where one of the stars has a planetesimal disc and we followed the planetesimals transferred to the star initially without a disc. Because we approximate the disc by zero-mass particles, the results will not change in case both stars have a disc.

2.1 Numerical method

We assumed that the masses of planetesimals are small compared to the stars (debris discs are typically less massive than 1 $M_\oplus$, for example, Wyatt 2008). Under this assumption we represented the planetesimals by zero-mass points. Such particles move in the gravitational potential of the two stars, they do not interact with each other and neither do they influence the motion of the two stars.

We integrate the equations of motions using a combination of *N*-body and hybrid methods (the same as in Jílková et al. 2015 and similarly as in Jílková & Portegies Zwart 2015). The orbit of the two stars is integrated using the symplectic *N*-body code HUAYNO (Pelupessy, Jänes & Portegies Zwart 2012). As long as the stars are well separated (at least three times the disc size), the orbits of the planetesimals around their parent star at the beginning of the encounter and around the encountering star in the later times, are calculated by solving Kepler's equations using universal variables (here we adopted the solver from the SAKURA code, Gonçalves Ferrari, Boekholt & Portegies Zwart 2014). In this hybrid approach, the gravitational influence of the other star is considered as a perturbation and is coupled to the planetesimals using BRIDGE (Fujii et al. 2007). All calculations and the coupling of codes are realized using the Astronomical Multi-purpose Software Environment or AMUSE (Pelupessy et al. 2013; Portegies Zwart et al. 2013).[1] During the initial stages of the flybys (when the distance between the stars is large and decreasing) the influence of the star initially without the disc is considered as a perturbation, while during the later stages (when the distance between the stars is large and increasing) the influence of the disc parent star is considered as a perturbation of the particles captured by the other star. By comparing with self-consistent *N*-body simulations in which all the particles are integrated directly, we tested that the hybrid approach treats the captured particles correctly. However during the later stages of the flyby, larger inaccuracies can be introduced in the orbits of the particles that are not captured by the other star, i.e. those particles that are still bound to the parent star or completely unbound from the system. In these cases, the influence of the parent star is comparable to or stronger that of the other star and the assumption of our hybrid method, that it can be considered as a perturbation, is not fulfilled. Our approach is appropriate only for the particles whose dynamics during the later stages of the encounter are dominated by the star initially without disc, the transferred particles, on which we focus here. This approximate approach allows us to carry out many fast simulations and map parameter space of the encounters systematically.

2.2 Initial conditions

We set the mass of the star without the disc, M_1, to 1 $M_\odot$ in all our simulations. We systematically varied the mass of the star initially with disc M_2, the pericentre of the encounter $q_{\rm enc}$, and the eccentricity of the encounter $e_{\rm enc}$, in the ranges of 0.1–2 $M_\odot$, 200–500 AU, and 1.001–4.5, respectively. These values correspond to encounters that occur in star clusters and associations (for example, Lestrade et al. 2011, and references therein). Here we restrict to mass ratios M_2/M_1 from 0.5 to 10. We note that encounters with higher mass ratios (up to few hundred) are also expected in clustered environment (for example, Olczak et al. 2010).

We further run simulations with different mutual inclination of the encounter plane and the plane of the disc (which is the plane of reference, see Fig. 1), $i_{\rm enc}$, and different argument of periastron of the encounter, $\omega_{\rm enc}$. Because the disc is axisymmetric, the third angle defining the mutual geometry of the orbit of the two stars and the disc – the longitude of ascending node – does not play a role. The initial conditions are illustrated in Fig. 1 and all the considered parameters values are specified in Table 1.

The initial separation of the encountering stars is set up in such way that the amplitude of the gravitational force from the parent star M_2 at the distance of outer edge of the disc (200 AU from the star of mass M_2) is 10 times larger than the amplitude of the gravitational force from the other star with mass M_1. Such an initial separation is sufficiently large and the influence of the star initially without the

[1] http://amusecode.org.

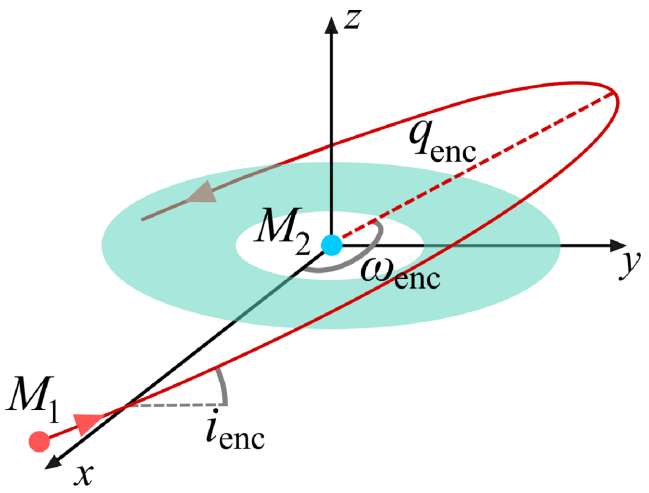

Figure 1. A doodle of the initial conditions of the encounter simulation. The red bullet indicates star M_1 which is initially without the disc, while the blue bullet indicates star M_2 and its disc is shown by the light green annulus. The coordinate system is centred on star M_2 and the reference plane xy is defined by the disc. The stars are moving on a parabolic orbit which is indicated by the full red line. The pericentre of the encounter q_{enc} is indicated by the dashed red line. The plane of the encounter is inclined by the inclination angle i_{enc} around the x-axis. The argument of pericentre ω_{enc} is measured in the encounter plane between the x-axis and the direction to the pericentre. The doodle is not scaled.

Table 1. Initial conditions for encounter simulations. The values of q_{enc}, M_2, and e_{enc} on first section define a grid of 1000 runs. Furthermore, the runs with i_{enc} and ω_{enc} varied are listed. The last section describes the cases when the eccentricity of the disc particles, e_{disc}, was varied.

Grid parameters:		
q_{enc}	(AU)	200, 220, 240, 260, 280, 300, 350, 400, 450, 500
M_2	($M_\odot$)	0.1, 0.2, 0.3, 0.4, 0.5, 0.75, 1.0, 1.25, 1.5, 2.0
e_{enc}		1.001, 1.25, 1.5, 1.75, 2.0, 2.5, 3.0, 3.5, 4.0, 4.5
i_{enc}	(°)	0
ω_{enc}	(°)	90
e_{disc}		0
Varying i_{enc}:		
q_{enc}	(AU)	200, 300
M_2	($M_\odot$)	0.1, 0.5, 1.0
e_{enc}		1.001, 1.5, 3.0
i_{enc}	(°)	0–180, in steps of 15
ω_{enc}	(°)	90
e_{disc}		0
Varying ω_{enc}:		
q_{enc}	(AU)	200
M_2	($M_\odot$)	0.1
e_{enc}		1.0
i_{enc}	(°)	30, 60, 90, 120
ω_{enc}	(°)	0–180, in steps of 15
e_{disc}		0
Varying e_{disc}:		
q_{enc}	(AU)	200, 300, 400
M_2	($M_\odot$)	0.1, 0.5, 1.0, 1.5
e_{enc}		1.001, 1.5, 3.0
i_{enc}	(°)	0
ω_{enc}	(°)	90
e_{disc}		0–0.05, 0–0.1

disc on the planetesimals is negligible. We tested that increasing the initial separation up to where the force at the outer disc edge from star M_1 is 1 per cent of the one from star M_2 (as used by Breslau et al. 2014) does not change the results (in agreement with Clarke & Pringle 1993; Hall et al. 1996). We integrate the encounter until the separation between the two stars again reaches the initial value. Hall et al. (1996) pointed out that most of the interactions between the disc particles and the perturber takes place shortly after the closest approach. We tested and confirmed that our integration time is sufficient for the captured particles to settle to their final state.

Planetesimals initially orbit star M_2 in a flat disc (that is we do not consider any vertical profile). Unless specified otherwise, we use 10^4 disc particles. By increasing the number of particles (up to 5×10^4) in several simulations, we tested that the results do not change for higher resolutions. For several specific encounters, we run simulations with six different values of the random seed. We estimate the error of our results by the standard deviations of the quantities we study below (such as the radii of the transfer region and the transfer efficiency, Section 3), which are smaller than 2 per cent for all the studied cases.

The initial radius and phase of the planetesimals in the disc are uniformly distributed, which corresponds to the surface number density $\propto 1/r$, where r is the radial distance of the particles from the parent star measured in the plane of the disc. Such a profile is often used to model protoplanetary discs (e.g. Steinhausen, Olczak & Pfalzner 2012; Pelupessy & Portegies Zwart 2013, and references therein) and is supported by observations (e.g. Andrews & Williams 2007). Since the disc is represented by zero-mass particles, it is possible to re-scale the surface number density profile in post-processing of the simulations to represent different initial surface mass density radial profiles. Each particle can be considered with a weight given by its initial radius so that the surface radial profile is a specific function of r (similarly as in Steinhausen et al. 2012). We discuss the role of the initial disc surface density in Section 3.7. We set the radial extent of the disc to 30–200 AU. Such choice is consistent with disc sizes typically observed in clustered environments (see for example, Vincke et al. 2015, and references therein). Unless specified otherwise, the planetesimals are initialized on circular orbits.

For most of our initial conditions, the disc and the orbit of the two stars are in the same plane and the z-components of their angular momentum have the same direction. Such a coplanar prograde case results in the most violent encounters and with the highest number of transferred particles. We carried out 1000 of such simulations and the grid of encounter parameters is given in the first section of Table 1. To estimate the effect of the general geometry, we varied the relative inclination of the plane of the encounter with respect to the disc, i_{enc}, and also the argument of periastron of the orbit of the two stars, ω_{enc}. We specify the encounter parameters in the second and third sections of the Table 1.

To estimate the effect of eccentricity of the planetesimals orbits, e_{disc}, we run simulations where the eccentricities are randomly selected from a uniform distribution from 0 to $e_{disc,max} = 0.05$ or 0.1 (see last section of Table 1).

3 RESULTS

In each encounter experiment, we follow the disc particles that are transferred from star M_2 to star M_1 (initially with and without disc, respectively). We calculate the orbital elements of the disc particles with respect to both stars – the semimajor axis, a_s, and

eccentricity, e_s, inclination, i_s, and argument of periastron, ω_s (see Section 3.4.1 for the discussion on the choice of the reference plane); where the index s identifies the star, that is $s = 1, 2$. We identify the captured particles as those bound only to the star M_1 at the end of the simulations. At the end of most of our simulations, a small fraction of the particles (typically less than 5 per cent) are bound to both stars. By increasing the integration time (more than five times) and using full N-body simulations, we tested that these particles generally become bound only to star M_2 or unbound from the system and do not change the characteristics of the captured population. To avoid low number statistics we consider only the simulations in which at least 100 particles are transferred (48 out of our 1000 coplanar prograde simulations result in 1–99 transferred particles).

We first focus on a description of the results of the systematic grid parameter space study (encounter parameters listed in the first part of Table 1, Sections 3.1–3.3) and later on the cases with a more general geometry (Sections 3.4 and 3.5), the case with an eccentric disc (Section 3.6), and we also consider the role of the surface density of the disc (Section 3.7)

3.1 Transfer region

The fate of a particle after the encounter is determined by its orbit in the initial disc around the parent star M_2. We identify a minimal disc radius from where the particles can be transferred to M_1. We call this radius $r_{\rm tr,min}$ and we show that it generally corresponds to the radius from where the particles can be unbound from the parent star M_2, $r_{\rm un,min}$. It was already pointed out by Kobayashi & Ida (2001) that $r_{\rm un,min}$ depends on the parameters of the encounter – the mass ratio M_1/M_2, pericentre $q_{\rm enc}$, and the eccentricity $e_{\rm enc}$ – as

$$r_{\rm un,min} \approx \alpha\,[(1 + M_1/M_2)(1 + e_{\rm enc})]^{(-1/3)}\,q_{\rm enc}, \qquad (1)$$

where $\alpha \approx 0.3$ or 0.5 for a prograde or retrograde encounter, respectively. Our results show similar trends and in Section 4, we provide a detailed description of a derivation of an approximate analytic formula for $r_{\rm tr,min}(M_1/M_2, q_{\rm enc}, e_{\rm enc})$ and compare it with the results from our simulations in Section 4.4.

In Fig. 2, we show the dependence of $r_{\rm tr,min}$ on the mass ratio of the encounter stars and the pericentre of the encounter for the coplanar prograde parabolic encounters (i.e. for which the highest number of particles is transferred). The initial radial extent of the disc is 30–200 AU (Section 2.2) which also sets the limits on $r_{\rm tr,min}$. For the cases with large pericentres ($q_{\rm enc} \gtrsim 450$ AU) and high-mass ratios ($M_2/M_1 \gtrsim 1.25$), $r_{\rm tr,min}$ is close to or larger than the initial disc extent of 200 AU; for smaller pericentres ($q_{\rm enc} \lesssim 200$ AU) and low-mass ratios ($M_2/M_1 \lesssim 0.1$), $r_{\rm tr,min}$ is decreasing up to the lower disc size limit of 30 AU. Fig. 2 demonstrates the dependence of $r_{\rm tr,min}$ on the pericentre of the encounter $q_{\rm enc}$ and the mass ratio M_2/M_1 and in Fig. 3, we show that the minimal transfer radius $r_{\rm tr,min}$ depends only weakly on the encounter eccentricity $e_{\rm enc}$ (in agreement with Kobayashi & Ida 2001).

For faster hyperbolic encounters (with eccentricities $e_{\rm enc} \gtrsim 2.5$), we also identify a maximal radius from up to where the particles are transferred to star M_1, $r_{\rm tr,max}$. For encounters with $e_{\rm enc} \lesssim 2.5$, the particles are transferred from up to the outer edge of the disc of 200 AU which corresponds to the lower limit on $r_{\rm tr,max}$. In Fig. 4, we show $r_{\rm tr,max}$ for coplanar prograde encounters with $e_{\rm enc} = 3.5$. As expected and similarly to $r_{\rm tr,min}$, $r_{\rm tr,max}$ also increases with larger mass ratios and larger pericentres.

In Fig. 5, we show the radial distribution of the relative number of transferred particles for the encounters with $M_2/M_1 = 0.75$ and $q_{\rm enc} = 240$ AU and for two different encounter eccentricities $e_{\rm enc} = 1.0$ and 3.5, which are also plotted in Figs 2 and 4. In the case of the slower, parabolic encounter, more particles are transferred from a wider radial range, where the outer edge is outside the initial extent of the disc (of 200 AU, see red diamonds and dashed line in Fig. 5) The faster encounter results in fewer transferred particles and $r_{\rm tr,max} < 200$ AU.

We note that in about 25 simulations (out of the total 1000), a small number of outlier particles (this is always $\lesssim$5 particles, which is never more than 5 per cent of the total number of the captured particles) are transferred from outside the initial disc region limited by $r_{\rm tr,min}$ and $r_{\rm tr,max}$. This is a result of the approximate hybrid approach when integrating the orbits of the disc particles (see

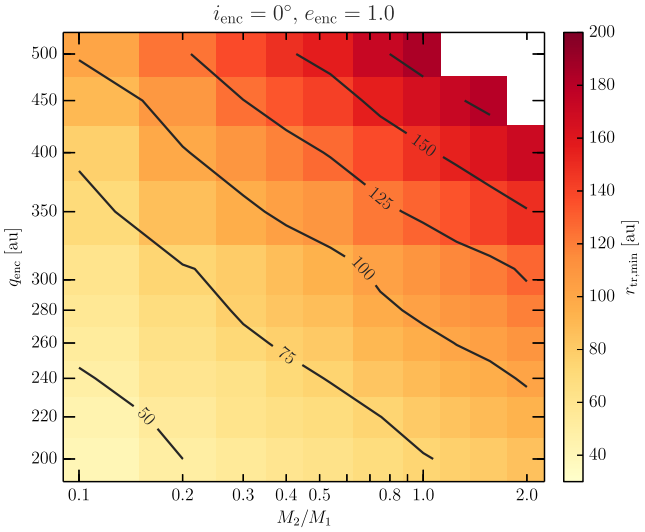

Figure 2. Minimal disc radius from where the particles can be transferred $r_{\rm tr,min}$ for coplanar prograde ($i_{\rm enc} = 0°$) parabolic ($e_{\rm enc} = 1.0$) encounters. The horizontal axis shows the mass ratio of star initially with to without disc M_2/M_1, the vertical axis shows the pericentre of the encounter $q_{\rm enc}$. Note that both horizontal and vertical axes are logarithmic. The colour scale maps the minimal transfer radius $r_{\rm tr,min}$. The contour levels are in AU.

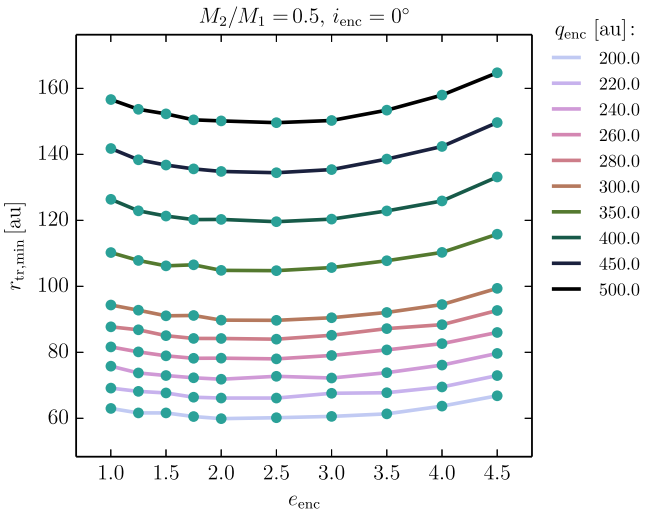

Figure 3. Minimal transfer radius, $r_{\rm tr,min}$, for encounters with mass ratio $M_2/M_1 = 0.5$ and different pericentres $q_{\rm enc}$ as a function of eccentricity, $e_{\rm enc}$. Here, $r_{\rm tr,min}$ for the parabolic orbits ($e_{\rm enc} = 1.0$) correspond to the values mapped in Fig. 2 for the mass ratio $M_2/M_1 = 0.5$ fixed on the horizontal axis.

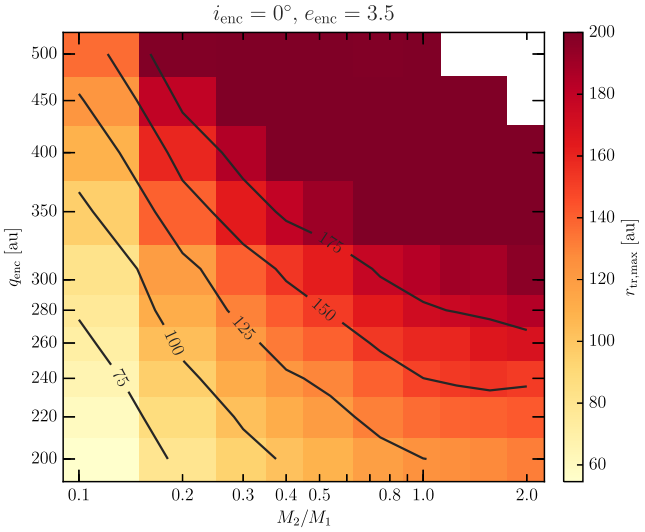

Figure 4. Maximal disc radius from where the particles can be transferred, $r_{tr,max}$, for coplanar prograde ($i_{enc} = 0°$) encounters with $e_{enc} = 3.5$. The horizontal axis shows the mass ratio of the stars M_2/M_1, the vertical axis shows the pericentre of the encounter. Note that both horizontal and vertical axes are logarithmic. The colour scale maps the $r_{tr,max}$. Here, 200 AU is the initial outer edge of the disc and therefore a lower limit of $r_{tr,max}$. The contour levels are in AU.

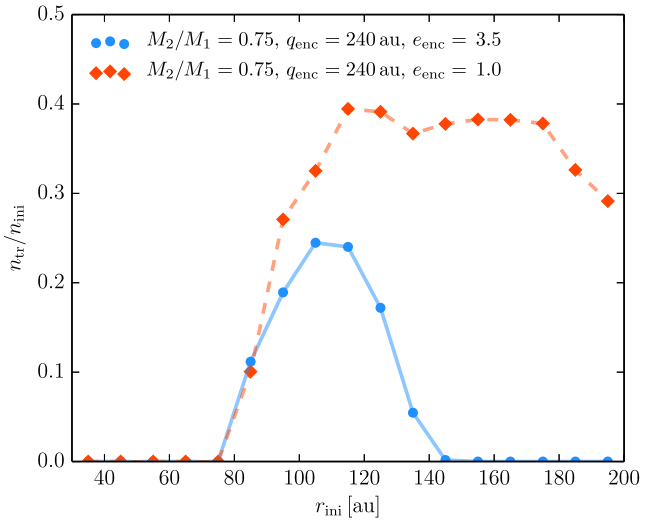

Figure 5. Radial distribution of the relative number of transferred particles for two coplanar prograde encounters with the same mass ratio ($M_2/M_1 = 0.75$) and pericentre ($q_{enc} = 240$ AU) and different eccentricities. The horizontal axis shows the initial disc radius of the particles r_{ini}. The distribution is calculated in equidistant radial bins of 10 AU. The ratio of the transferred (n_{tr}) to the initial (n_{ini}) number of particles in each bin is shown on the vertical axis. Blue bullets connected by solid line and red diamonds connected by dashed line correspond to the encounter eccentricity of 1.0 and 3.5, respectively.

Section 2.1) and we tested the method correcting for the outliers by comparing with the *N*-body simulations.

The initial position in the disc for the particles of different final fate is showed in Fig. 6, for the encounter with $M_2/M_1 = 0.75$, $q_{enc} = 240$ AU, and $e_{enc} = 3.5$ (same encounter as already shown in Fig. 5 in the red distribution). We show the initial disc around star M_2 colour-coded by the fate of the particles after the encounter in the left-hand panel of Fig. 6; and the radial distributions of the relative number of the particles in the right-hand panel. Most of the particles, 74 per cent of the initial 10^4, stay bound to the parent star; 18 per cent are unbound from the system and lost into interstellar space; 6 per cent are transferred to star M_1; and 2 per cent are left bound to both of the stars. The small number of particles that are bound to both stars (shown in violet) is initially spread over the whole radial extent of the disc; these particles will typically end-up unbound from the system or bound only to star M_2. As can be seen from the blue radial distribution in Fig. 5, the transferred particles (shown in dark blue) are initially enclosed in between two radii. Similarly, the particles that are eventually unbound from the system (shown in green) are limited by a minimal radius, called $r_{un,min}$, that is very similar to the minimal radius of the transferred particles $r_{tr,min}$. In Fig. 7, we show the relative difference between $r_{tr,min}$ and $r_{un,min}$ (the latter is always smaller than the former). The difference between the two minimal radii is less than 8 per cent of $r_{tr,min}$ for all the encounter with $e_{enc} \lesssim 3.5$, and less than 15 per cent for the cases with higher eccentricities. This might result from the faster encounters generally producing a smaller number of transferred particles.

3.2 Transfer efficiency

To measure the efficiency of the transfer we follow the ratio of the number of transferred particles and the number of particles initially located in the original disc within the range $r_{tr,min}$–$r_{tr,max}$. We call this quantity the transfer efficiency, μ_{tr}. It is important to keep in mind that as showed in Section 3.1, for a substantial part of the studied parameter space, the maximal disc radius of the transferred particles $r_{tr,max}$ is larger than the considered outer edge of the disc of 200 AU. The complete transfer region of transfers is not covered for these cases.

In Figs 8 and 9, we present μ_{tr} for the pericentres q_{enc}, and mass ratios M_2/M_1, of the encounter for fixed eccentricities e_{enc} of 1.0 and 3.5, respectively. We mark the encounters for which the transfer region is not completely covered (i.e. $r_{tr,max} > 200$ AU) by the red cross. Regardless of the incompleteness of the data, lower mass ratios result in higher transfer efficiencies. This is consistent with the conclusion of Pfalzner et al. (2005a, note that they defined the mass ratio of the encountering star inverse to the one used here). However, for eccentric orbits (Fig. 9), the encounters with the lowest considered mass ratio $M_2/M_1 = 0.1$, have a lower transfer efficiency than encounters with $M_2/M_1 = 0.2$. The same feature is present for all higher encounter eccentricities $e_{enc} \gtrsim 3.0$. By increasing the number of the disc particles (to 5×10^4) and by decreasing the initial disc extent (so that the inner and outer disc edges are closer to the values of $r_{tr,min}$ and $r_{tr,max}$, respectively), we tested that this result is not resolution dependent. To increase the resolution in the mass ratio M_2/M_1 of our grid, we also run additional simulations with $M_2/M_1 = 0.125$, 0.15, and 0.175 $M_\odot$ for the encounters with $e_{enc} = 3.5$, and we find that the transfer efficiency μ_{tr} is indeed lowest for the $M_2/M_1 = 0.1$ and smoothly increasing up to $M_2/M_1 = 0.2$. The transfer efficiency is generally higher for the parabolic encounters ($\mu_{tr} = 0.1$–0.23 for $e_{enc} = 3.5$ in Fig. 9 while $\mu_{tr} = 0.15$–0.45 for $e_{enc} = 3.5$ in Fig. 8) as was already noted by Pfalzner et al. (2005b).

Regarding the dependence of μ_{tr} on the pericentre of the encounter q_{enc}, Figs 8 and 9 indicate that the transfer ratio is maximal for a particular value of q_{enc} which is the same for different mass ratios – 260 AU for the parabolic encounters (Fig. 8) and ∼350–400 AU for $e_{enc} = 3.5$ (Fig. 8). In Fig. 10, we show the dependence of μ_{tr} on q_{enc} for encounters with a fixed mass ratio but a range in

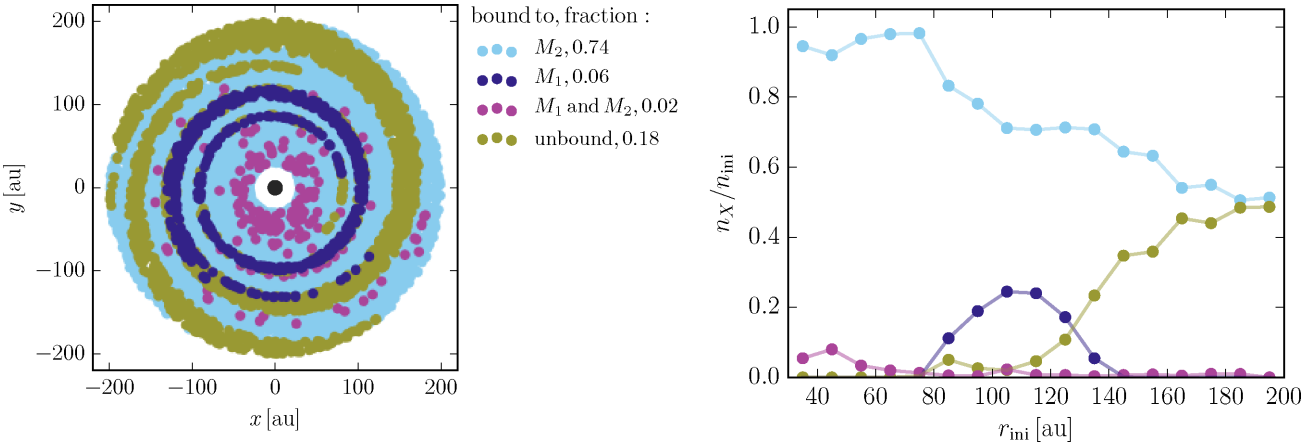

Figure 6. Initial distribution of the disc for different fate of the particles for the encounter with $M_2/M_1 = 0.75$, $q_{\rm enc} = 240$ AU, and $e_{\rm enc} = 3.5$. Left: the plane of the disc with the coordinates in a non-inertial reference frame centred on the star M_2 (marked by black bullet in the centre). Disc particles are colour-coded according to their final fate after the encounter as indicated in the legend where the fraction for each option is also given. Right: relative distributions of the initial disc radius of the particles of different final status. The distributions are calculated in equidistant radial bins of 10 AU. The ratio of the number of particles (n_X, where X stands for bound to M_2 or/and M_1 or unbound from the system) to the initial ($n_{\rm ini}$) number of particles in each bin is shown on the vertical axis.

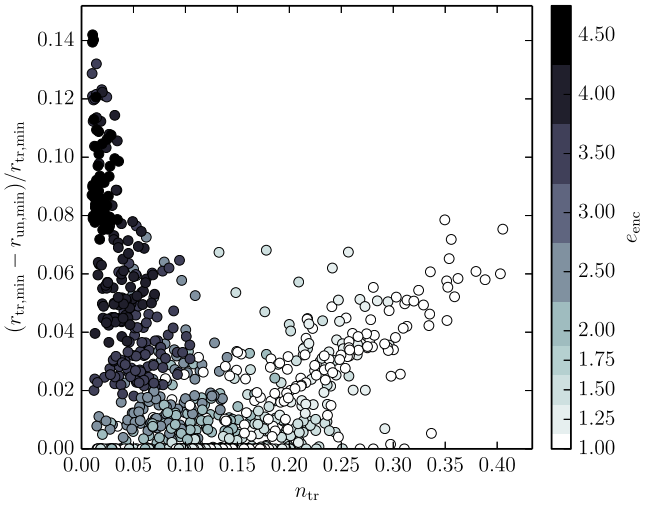

Figure 7. Relative difference between the minimal transfer radius $r_{\rm tr,min}$, and the minimal radius of the unbound particles $r_{\rm un,min}$, as a function of the relative number of transferred particles $n_{\rm tr}$ for the 1000 encounters of the parameters grid. Coplanar encounters are plotted and colour-coded by the eccentricity $e_{\rm enc}$ (regardless the pericentre $q_{\rm enc}$ and mass M_2).

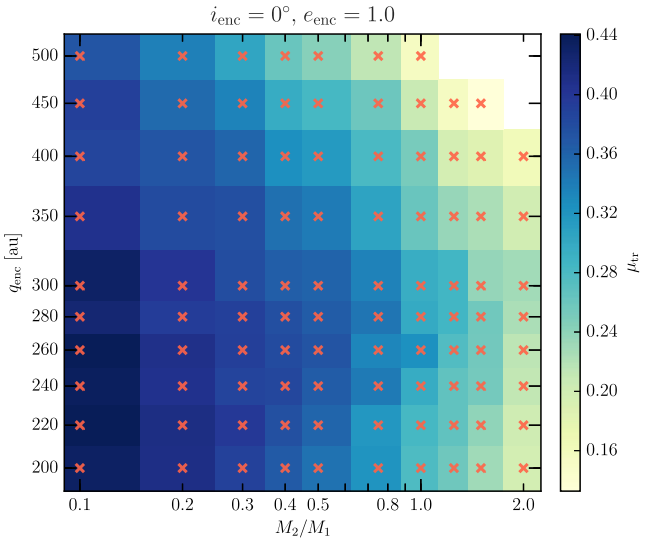

Figure 8. Efficiency of mass transfer $\mu_{\rm tr}$ for coplanar prograde parabolic encounters. The horizontal axis shows the mass ratio M_2/M_1, the vertical axis shows the pericentre of the encounter $q_{\rm enc}$. Note that both horizontal and vertical axes are logarithmic. The colour scale maps the $\mu_{\rm tr}$. The red crosses mark the bins where $r_{\rm tr,max} > 200$ AU and the transfer region is not completely covered – which is the case for all encounters here.

eccentricities. The transfer efficiency is higher at larger pericentre for higher values of $e_{\rm enc}$. Regardless of the pericentre, the transfer efficiency is generally smaller for more eccentric encounters.

In previous studies, the number of transferred particles was followed rather than its ratio to the initial population in the transfer region, that is than what we call the transfer efficiency $\mu_{\rm tr}$. In Fig. 11, we plot the number of transferred particles as the fraction of the total number of disc particles, $n_{\rm tr}$. Fig. 11 has the same setup as Fig. 10, where the mass ratio is fixed and the dependence on the encounter pericentre is shown for different eccentricities. Most of the previous work focused on the case of a coplanar prograde parabolic orbit which leads the most efficient transfer for any given mass ratio and pericentre. The number of transferred particles $n_{\rm tr}$ decreases almost linearly with $q_{\rm enc}$ in this case in agreement with Pfalzner et al. (2005a). This is furthermore confirmed in Fig. 12, where we plot $n_{\rm tr}$ for all the coplanar prograde parabolic encounters for different M_2/M_1. The linear decrease has an approximately constant slope irrespective of the masses of the stars, while is generally lower for higher mass ratios (that is for large masses of the star initially with the disc, M_2).

The number of transferred particles as well as the transfer efficiency can in principle depend on the surface number density profile of the disc particles. As mentioned in Section 2.2, we adopted an initial uniform distribution in r which corresponds to the surface density $\propto 1/r$. To address this effect, we consider different surface density profiles in Section 3.7.

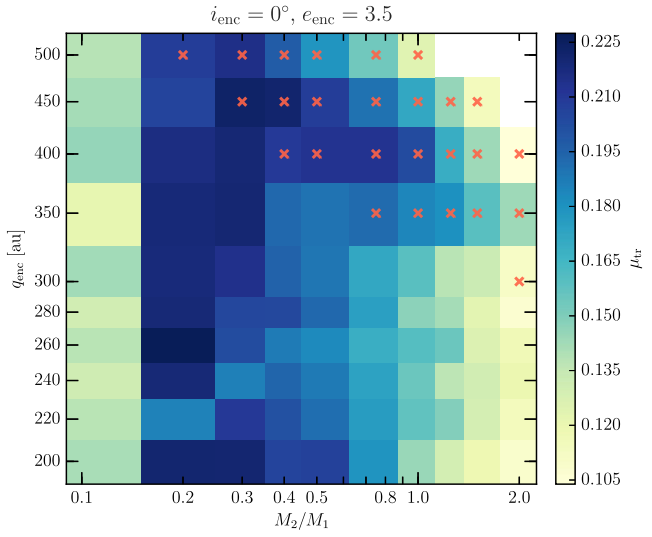

Figure 9. Efficiency of mass transfer μ_{tr} for coplanar prograde encounters with an eccentricity of 3.5. See Fig. 8 for a detailed description.

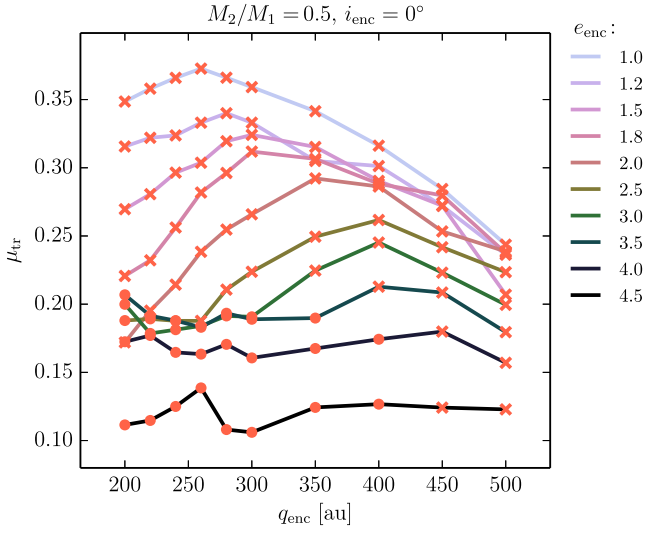

Figure 10. Dependence of the efficiency of mass transfer μ_{tr} on the pericentre of the encounter q_{enc}. The encounters are coplanar and prograde encounters with mass ratio $M_2/M_1 = 0.5$. Lines of different colours correspond to different encounter eccentricities, e_{enc}, as indicated to the right. Bullets depict the encounters with completely covered transfer region, while crosses the encounters with $r_{tr,max} > 200$ AU.

3.3 Orbits of the transferred planetesimals

The transferred particles represent a specific population in orbit around their new host M_1. In this section, we analyse the orbits of particles transferred in coplanar prograde encounters ($i_{enc} = 0°$), these are described in Sections 3.1 and 3.2. Orbits of particles transferred during encounters with non-zero inclination of the disc and the plane of the encounter, i_{enc}, are described in Sections 3.4 and 3.5.

In Fig. 13, we show the minimal semimajor axis of the transferred particles $a_{1,min}$ (which corresponds to the transferred orbit with the minimal energy) as a function of the mass ratio M_2/M_1, and the pericentre of the encounter q_{enc} for the parabolic prograde coplanar encounters ($e_{enc} = 1.0$, $i_{enc} = 0°$). There is a clear trend – as expected, for larger pericentre and smaller mass ratio, the larger $a_{1,min}$.

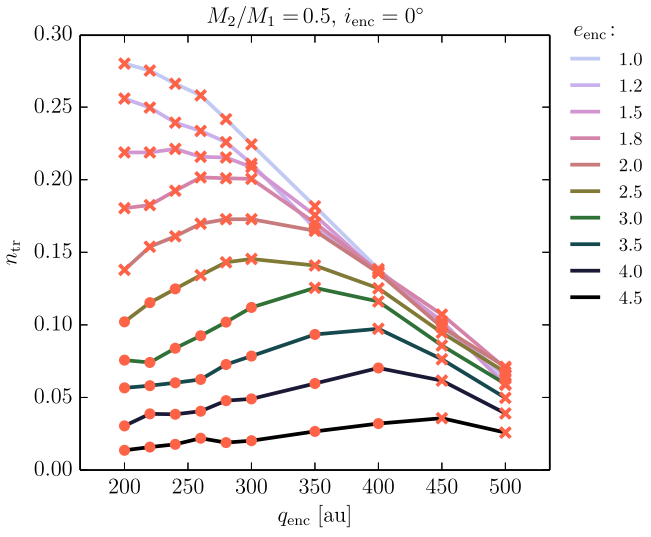

Figure 11. Dependence of the relative number of the transferred particles n_{tr} on the pericentre of the encounter q_{enc} for mass ratio $M_2/M_1 = 0.5$, and different eccentricities e_{enc}. See Fig. 10 for a detailed description.

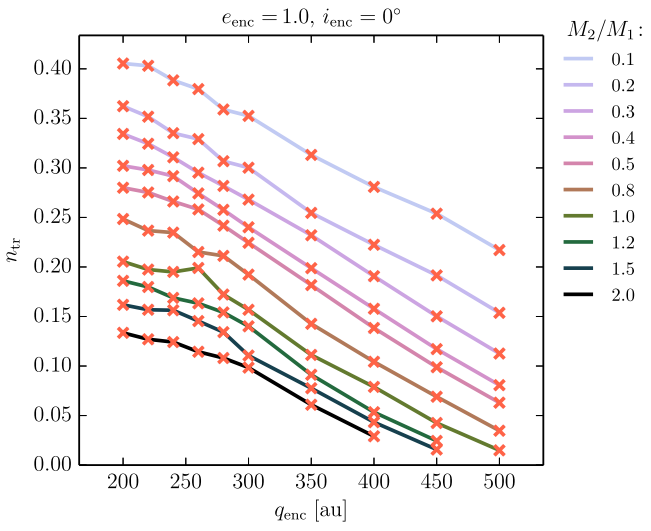

Figure 12. Dependence of the relative number of the transferred particles n_{tr} on the pericentre of the encounter q_{enc} for coplanar prograde parabolic encounters for different mass ratio M_2/M_1. Similarly to Fig. 10, lines of different colours correspond to different mass ratios M_2/M_1, as indicated to the right. Here, points are indicated by crosses because the transfer region is not completely covered for any of the displayed simulations (i.e. $r_{tr,max} > 200$ AU, see Fig. 10).

In Fig. 14, we show $a_{1,min}$ as a function of q_{enc} for different e_{enc} and fixed M_2/M_1. The minimal semimajor axis of the transferred orbits $a_{1,min}$ is a linear function of the pericentre of the encounter q_{enc} and the coefficient of the proportionality depends on the eccentricity of the encounter e_{enc} – larger values of e_{enc} result in steeper increase of $a_{1,min}$ with q_{enc}.

Most of the transferred particles are on eccentric orbits (Pfalzner et al. 2005b). In Fig. 15, we show the eccentricity distributions of the transferred particles for coplanar prograde encounters. Similarly to Pfalzner et al. (2005b, their fig. 7, bottom), for the parabolic encounters the captured particles move on eccentric orbits with $e_1 \gtrsim 0.8$ irrespective of the pericentre q_{enc} and the mass ratio M_2/M_1 (Fig. 15, left and middle). The median eccentricity is generally

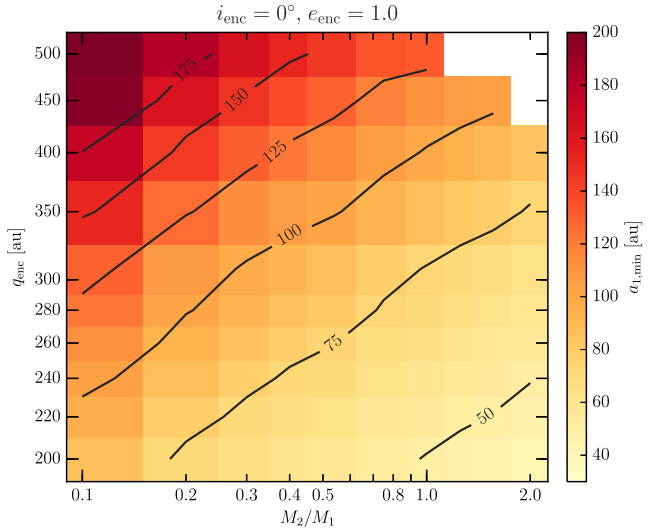

Figure 13. Minimal semimajor axis of the transferred particles for the coplanar prograde parabolic encounters ($e_{enc} = 1.0$, $i_{enc} = 0°$). The mass ratio M_2/M_1 and the pericentre of the encounter q_{enc} is increasing along the horizontal axis and vertical axis, respectively. Note that both horizontal and vertical axes are logarithmic. The colour scale maps the minimal semimajor axis of the orbits transferred around the star M_1. The contour levels are in AU.

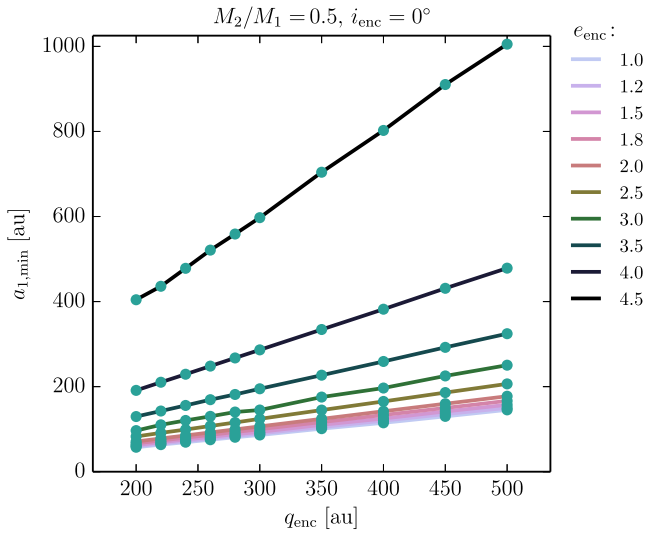

Figure 14. Minimal semimajor axis of the transferred particles $a_{1,min}$ as a function of the pericentre of the encounter q_{enc} for different eccentricities e_{enc} of coplanar prograde encounters. The mass ratio M_2/M_1 is 0.5 for all the depicted encounters. Lines of different colours show $a_{1,min}(q_{enc}, M_2/M_1 = 0.5, e_{enc})$ for fixed e_{enc} as indicated on the right-hand side of the plot.

decreasing with q_{enc} (red crosses in Fig. 15, left) and increasing with M_2/M_1 (red crosses in Fig. 15, middle). For the parabolic encounters ($e_{enc} = 1.0$, Fig. 15, left and middle), a small fraction of the captured particles (about 5 per cent or less) also have low eccentricities, $e_1 \lesssim 0.2$. For hyperbolic encounters ($e_{enc} > 1.0$) shown in Fig. 15, right, some of the transferred particles have relatively low eccentricity. For fixed q_{enc} and M_2/M_1, the median value of e_1 is decreasing with the encounter eccentricity up to $e_{enc} \sim 2.5$, and increasing again for more eccentric encounters. We find a similar dependence irrespective of the encounter pericentre q_{enc} and mass ratio M_2/M_1. In Fig. 16, we show the median value of the transferred particles' eccentricity $e_{1,med}$ as a function of e_{enc} for encounters with pericentre $q_{enc} = 500$ AU and different mass ratio M_2/M_1. We find that the median of e_1 is generally lower than 0.5 if the encounter pericentre is large, $q_{enc} \gtrsim 350$ AU.

3.4 Inclination of the encounter plane

To explore how the transfer efficiency and the characteristics of the captured population depend on the inclination of the disc plane with respect to the plane of the encounter i_{enc}, we carried out simulations with i_{enc} in the range of 0°–180° (see Table 1, section varying i_{enc}).

In Fig. 17, we show the dependence of the minimal transfer radius $r_{tr,min}$ on the encounter inclination i_{enc} for eight cases with different pericentre q_{enc}, mass ratio M_2/M_1, and eccentricity e_{enc}. In general, the minimal transfer radius $r_{tr,min}$ is increasing with inclination. For most of the encounter parameters we explored here, $r_{tr,min}$ increases beyond the outer edge of the disc of 200 AU for i_{enc} of about 60°. In the case of the encounter with $q_{enc} = 200$ AU, $M_2/M_1 = 0.5$, and $e_{enc} = 1.5$ (points connected by the orange line), $r_{tr,min} > 200$ AU for the orthogonal geometry ($i_{enc} = 90°$), while for $i_{enc} \approx 105°$–$150°$, $r_{tr,min}$ is smaller than 200 AU (decreasing for $i_{enc} \approx 105°$–$120°$ and increasing again for $i_{enc} \gtrsim 120°$).

As we describe in Section 3.1 and shown in Fig. 3, for given q_{enc} and M_2/M_1 the minimal transfer radius $r_{tr,min}$ does not strongly depend on the eccentricity e_{enc}. This changes with increasing inclination – the encounters with higher eccentricity e_{enc} have also larger minimal transfer radius $r_{tr,min}$.

Similarly as for the coplanar prograde encounters in Fig. 7, the minimal radius of the transferred particles $r_{tr,min}$ and the minimal radius or the unbound particles $r_{tr,min}$ do not differ by more than about 10 per cent for the inclined encounters.

The dependence of the transfer efficiency μ_{tr} on the encounter inclination i_{enc} is shown in Fig. 18. The relative number of transferred particles is expected to decrease with i_{enc} (Clarke & Pringle 1993) and we find a similar trend – the transfer efficiency μ_{tr} is generally also smaller for higher i_{enc}. Since $r_{tr,min}$ increases steeply for encounters with $i_{enc} > 90°$, our simulations do not cover the transfer region for most of the considered encounters.

Realistic encounters have random inclination i_{enc} and the results presented in the previous sections, which assumed that the disc and the encounter are in the same plane (i.e. coplanar geometry), represent the lower limits for the minimum transfer radius $r_{tr,min}$ (Fig. 17) and the upper limits for the transfer efficiency μ_{tr} (Fig. 18). Additionally, Figs 17 and 18 show that $r_{tr,min}$ and μ_{tr} in the low inclination ($i_{enc} \lesssim 30°$) encounters hardly differ from those in their respective co-planar cases for most parameters.

3.4.1 Orientation of the transferred orbits

For the coplanar encounters, all the transferred particles are orbiting their new host M_1 in the same plane – the plane of the disc and of the encounter orbit. The situation is different for the encounters that are inclined with respect to the disc plane, that is $i_{enc} > 0°$. Orbits are traditionally characterized by orbital elements, and in Section 3.3, we studied the distributions of the semimajor axes and eccentricities of the particles transferred in the coplanar prograde encounters. The orientation of the orbital plane with respect to a given reference plane can be defined by the inclination and the longitude of ascending node, and the orientation of the orbit in the

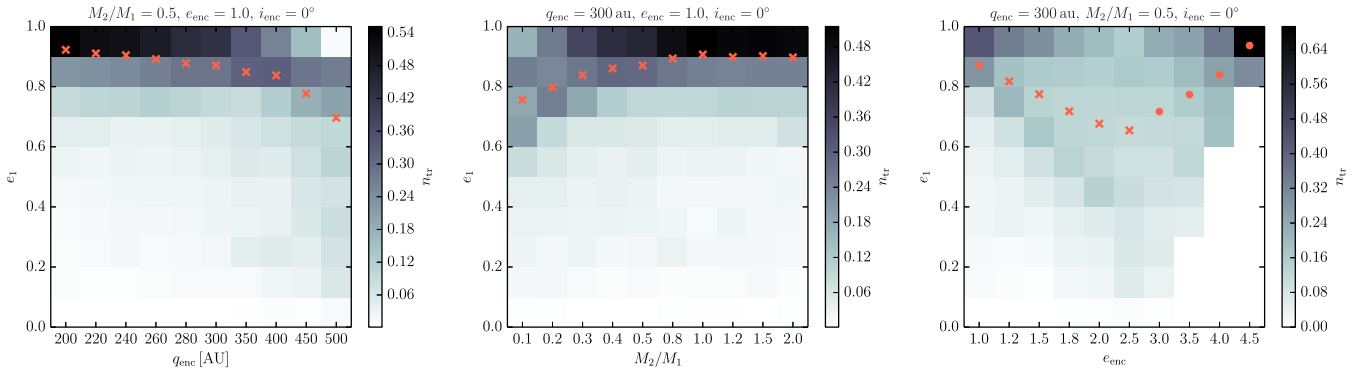

Figure 15. Distributions of the eccentricity of the transferred particles e_1 for coplanar prograde encounters ($i_{enc} = 0°$). The three plots show eccentricity distributions for different encounter pericentre q_{enc} (left), mass ratio M_2/M_1 (middle), and encounter eccentricity e_{enc} (right). Left: eccentricity distributions for encounters with $M_2/M_1 = 0.5$, $e_{enc} = 1.0$ (parabolic encounters), and q_{enc} varying along the horizontal axis. For clarity, the scale of the horizontal axis is arbitrary – values of pericentre are equidistantly distributed over the horizontal axis. The vertical axis shows the eccentricity of the transferred particles e_1 in 10 equidistant bins. The colour scale maps the relative number of transferred particles in each eccentricity bin as measured for individual encounters with different q_{enc}. The red symbols correspond to the median value of e_1. Bullets depict the encounters with completely covered transfer region, while crosses the encounters with $r_{tr,max} > 200$ AU (see Section 3.1 and, e.g. Fig. 10). Middle: eccentricity distributions for encounters with $q_{enc} = 300$ AU, $e_{enc} = 1.0$ (parabolic encounters), and different M_2/M_1 along the horizontal axis. Right: eccentricity distributions for encounters with $q_{enc} = 300$ AU, $M_2/M_1 = 0.5$, and different e_{enc} along the horizontal axis. The distribution at the $q_{enc} = 300$ on the horizontal axis of the left-hand plot, $M_2/M_1 = 0.5$ of the middle plot, and $e_{enc} = 1.0$ of the right one, is the same.

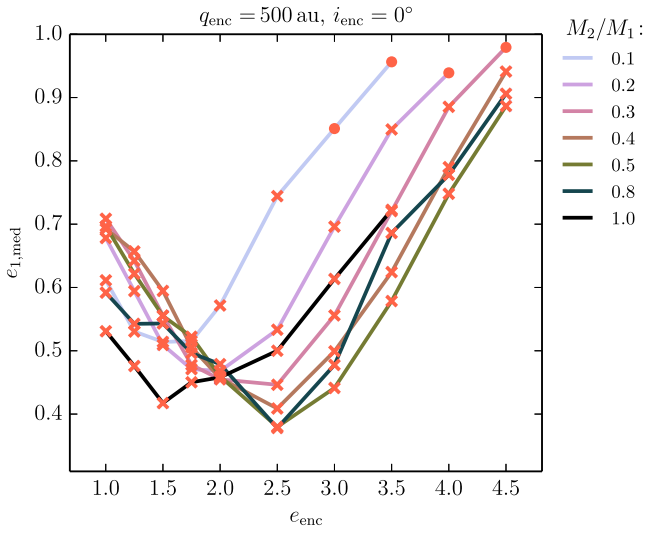

Figure 16. Median value of the eccentricity of the transferred particles $e_{1,med}$ as a function of the encounter eccentricity e_{enc} for coplanar prograde encounters with pericentre $q_{enc} = 500$ AU. The lines of different colours correspond to encounters with stars of different mass ratios M_2/M_1, as indicated on the right. Bullets depict the encounters with completely covered transfer region, while crosses the encounters with $r_{tr,max} > 200$ AU (see Section 3.1).

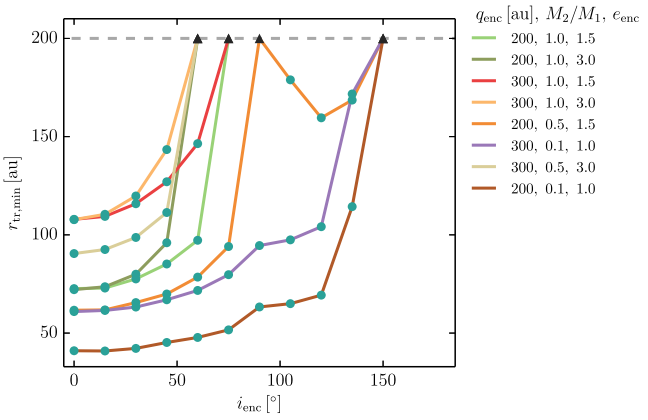

Figure 17. Minimal transfer radius $r_{tr,min}$ as a function of the encounter inclination i_{enc}. Eight encounters with different pericentre q_{enc}, mass ratio M_2/M_1, and eccentricity e_{enc}, are shown by lines of different colours, as indicated on the right. Note that for some encounters with higher i_{enc}, we used more particles (up to 5×10^4) and we used a larger value of the inner edge of the disc (while still smaller than $r_{tr,min}$, that is from the range 30 AU–$r_{tr,min}$) to increase the resolution. The grey dashed line at 200 AU is the upper limit on $r_{tr,min}$ given by the outer disc radius used in our simulations. The black triangles indicate the encounters for which no particles were transferred in our high-resolution simulations and therefore we assume that $r_{tr,min} > 200$ AU for these cases. The argument of periastron of the encounter ω_{enc} is 90° for all encounters.

orbital plane is defined by the argument of periastron. The plane of reference is in principle arbitrary and the orbital elements will differ based on the choice. Therefore we study the orientation of the orbital planes of the transferred particles using their angular momentum vectors.

The orbital plane is defined by the plane perpendicular to the specific relative angular momentum vector $\boldsymbol{h}$ of the orbiting body (cross product of the relative position and velocity vectors of the particles and star M_1). To describe the alignment of the orbital planes of the transferred particles, we study the clustering of the directions of their $\boldsymbol{h}$. We calculate the mean relative angular momentum vector of the transferred population $\boldsymbol{h}_{tr,mean}$ as the mean vector of normalized $\boldsymbol{h}$ of the transferred particles with respect to star M_1. We calculate the angles between $\boldsymbol{h}_{tr,mean}$ and $\boldsymbol{h}$, which we call ϕ_{tr}. The distribution of ϕ_{tr} then characterizes the clustering of the directions of $\boldsymbol{h}$, and therefore also the alignment of the orbital planes of the transferred particles. If the individual orbital planes have a similar orientation, we expect the angles ϕ_{tr} to be small.

In Fig. 19, we show the cumulative distribution functions of ϕ_{tr} for the particles transferred during our inclined encounters (see Table 1, section varying i_{inc}, and Figs 17 and 18). For 95 per cent of the encounters (41 out of 43 simulations), half of the transferred

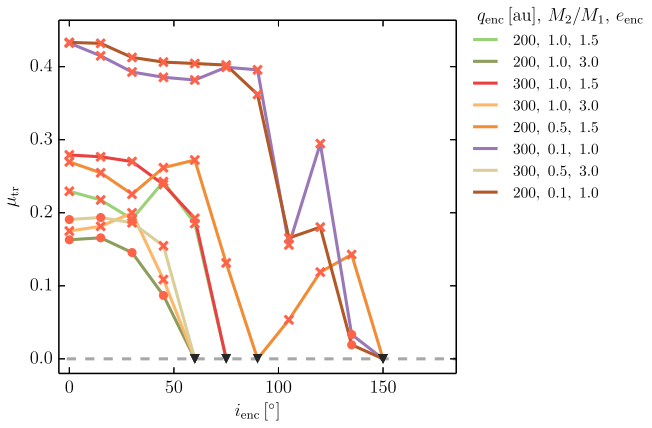

Figure 18. Transfer efficiency μ_{tr} as a function of encounter inclination i_{enc}. See Fig. 17 for a detailed description. The grey dashed line corresponds to no transferred particles and the black triangles indicate the high-resolution simulations where no particles were transferred. Bullets depict the encounters with completely covered transfer region, while crosses the encounters with $r_{tr,max} > 200$ AU (see Section 3.1).

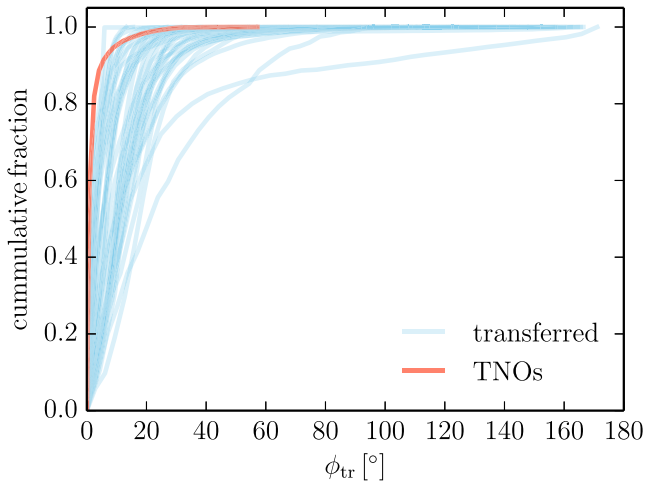

Figure 19. Cumulative distributions of ϕ_{tr} for the inclined encounters and for TNOs. Blue lines show the distributions for simulated transferred particles for the 48 inclined encounters plotted in Figs 17 and 18. Red line shows the distribution for the TNOs of the Solar system.

particles orbit in a plane with $\phi_{tr} \lesssim 15°$. The same limit on ϕ_{tr} also holds for 84 per cent of the particles in 36 out of 43 simulations.

For comparison, we carried the analysis for 1351 Transneptunian Objects of the Solar system (TNOs, bodies that orbit the Sun with average distance larger than Neptune's semimajor axis of 30 AU).[2] For more than 90 per cent of the TNOs, $\phi_{tr} < 5°$. The cumulative distribution of ϕ_{tr} is also plotted in Fig. 19 (red line). The orbital planes of the observed TNOs have a more similar orientation than the particles transferred in our simulations.

We calculated the orbital elements of the transferred orbits in the coordinate system with the plane of reference perpendicular to the mean vector of the normalized $\boldsymbol{h}$ of the captured particles. Regardless of the encounter parameters, the median values of the inclination of the captured population are typically $\lesssim 30°$ with standard deviations $\lesssim 35°$. The median values of the argument of pericentre are within the range from $-30°$ to $30°$, with the standard deviations $\sim 100°$. However, we observe that the argument of pericentre generally clusters in narrower distributions for the orbits captured at larger semimajor axes.

The transferred particles have specific distributions in the space of orbital elements and these are given by the parameters of the encounter (see also Section 3.3). In Fig. 20, we show distributions of the orbital elements of the captured population for encounters with a range in encounter inclination i_{enc} and eccentricity e_{enc}. The transferred population clearly depend on both parameters. For example, the last line of the mosaic shows encounters with $e_{enc} = 2.5$. Here, the distribution of semimajor axis a_1 and eccentricity e_1 are moving to higher values with increasing encounter inclination i_{enc} (see the bottom panels of the plots in the last line of the mosaic); the orbits also have higher inclination i_1 (middle panels); and the range of argument of pericentre ω_1 of the transferred orbits is shrinking (top panels). Each encounter parameter effects the captured population and its final distribution in the orbital elements space is given by a complex combination of the individual signatures. The population of the transferred particles can therefore be used to constrain the encounter through which it was delivered (Jílková et al. 2015).

3.5 Argument of periastron of the encounter

We investigated the role of the argument of periastron of the encounter ω_{enc} on the transfer region and efficiency. We carried out simulations sampling ω_{enc} in the range of 0°–180° for different inclinations i_{enc} and fixed pericentre $q_{enc} = 200$ AU, mass ratio $M_2/M_1 = 0.1$, and eccentricity $e_{enc} = 1.0$ (see Table 1, section varying ω_{enc}). Within the considered resolution, these encounter parameters result in mass transfer for inclinations $i_{enc} \leq 135°$ (Figs 17 and 18). In Fig. 21, we show the minimal disc radius of the transferred particles $r_{tr,min}$ and the transfer efficiency μ_{tr} as a function of ω_{enc} (top and bottom plot, respectively). The minimal radius $r_{tr,min}$ is independent of ω_{enc} for the prograde inclinations $i_{enc} \leq 90°$. For the retrotrograde encounters, $r_{tr,min}$ has a clear minimum for $\omega_{enc} \approx 105°$. The transfer efficiency μ_{tr} changes with ω_{enc} for all the considered inclinations $i_{enc} > 30°$. The higher i_{enc}, the larger the variations of μ_{tr}. Except for the encounter with the retrograde inclination $i_{enc} = 135°$ and regardless of i_{enc}, the transfer efficiency is approximately constant for $\omega_{enc} \lesssim 45°$ and $\gtrsim 150°$ and maximal for $\omega_{enc} \approx 90°$. This can be understood given the geometrical meaning of the argument of periastron ω_{enc} (Section 2.2, Fig. 1) – during the encounters with $\omega_{enc} \approx 90°$, the star M_1 passes at smaller distance to the disc particles for a longer time and captures more particles.

3.6 Eccentricity of the planetesimal disc

We studied the effect of the initial eccentricity of the disc e_{disc} on the transfer region and efficiency. For the encounters specified in the section varying e_{disc} of Table 1, we set up the initial eccentricities of the disc particles randomly with a uniform distribution within the ranges 0.0–0.05 and 0.0–0.1 and their orbital phase within 0 and 2π.

For most of the studied encounters, there is no substantial change due to the eccentricity of the disc particles e_{disc}. The minimal radius of the transferred particles $r_{tr,min}$, typically decreases by ∼5 per cent and 10 per cent compared to the

[2] We obtained the list of TNOs from the Minor Planet Center (MPC) data base operated at the Smithsonian Astrophysical Observatory under the auspices of the International Astronomical Union; http://www.minorplanetcenter.net/iau/lists/TNOs.html.

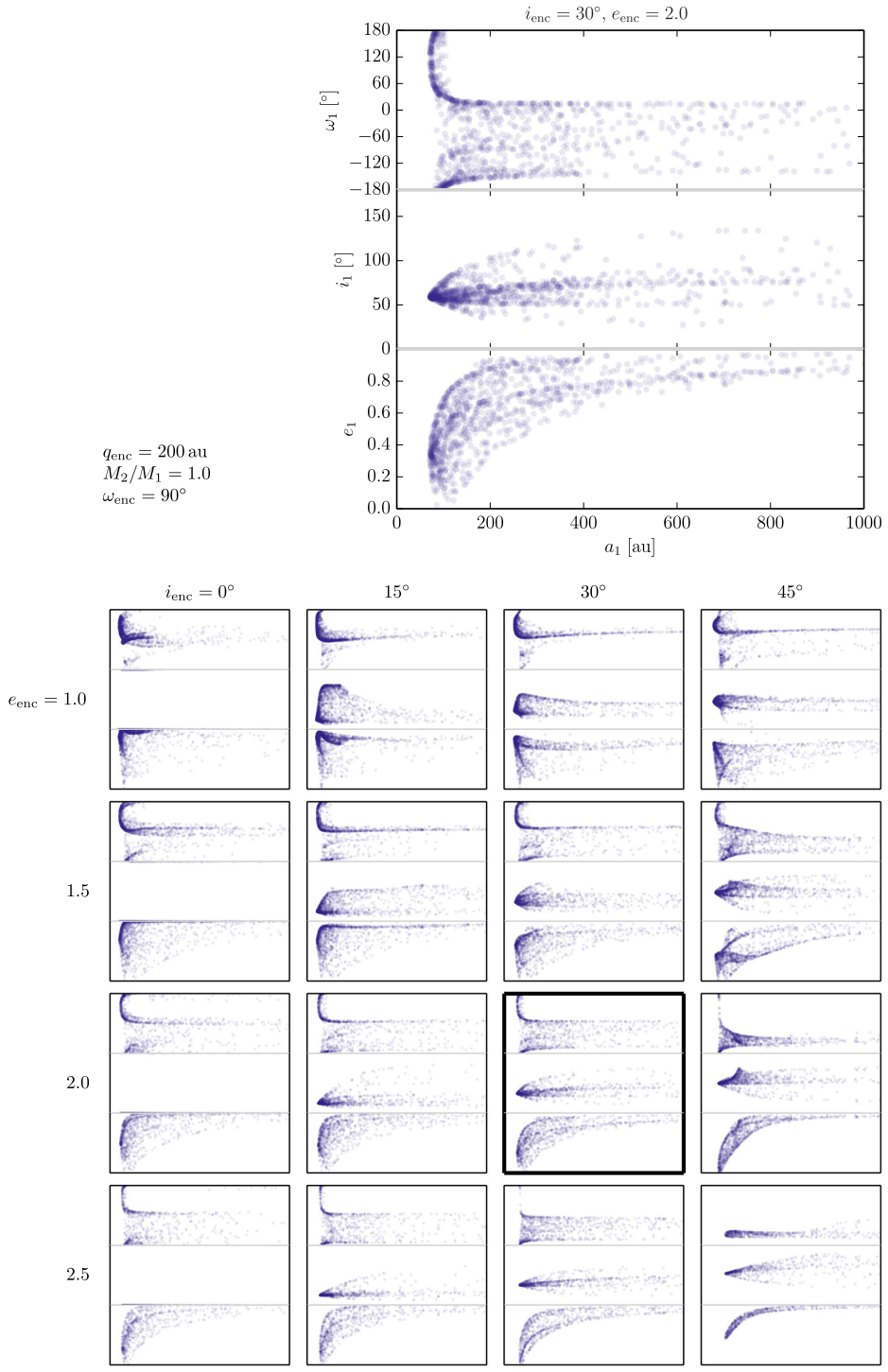

Figure 20. Orbital elements of the transferred particles. Each plot shows the argument of pericentre ω_1, the inclination i_1, and the eccentricity e_1 versus the semimajor axis a_1 of the transferred particles which are shown in the upper, middle, and bottom panel, respectively. All plots are for encounters with pericentre $q_{enc} = 200$ AU, mass ratio $M_2/M_1 = 1.0$, and argument of pericentre $\omega_{enc} = 90°$, while the encounter inclination i_{enc} and eccentricity e_{enc} vary. i_{enc} is changing along the columns, while e_{enc} along the rows of the mosaic of the small plots. The large plot shows the encounter with $i_{enc} = 30°$ and $e_{enc} = 2.0$ and is the same as the small plot highlighted with the thicker frame. All the plots cover the same ranges for all the variables (that is $a_1 = 0$–1000 AU on the horizontal axis, $e_1 = 0$–1 on the vertical axis of the lower panel, $i_1 = 0°$–$180°$ in the middle panel, and $\omega_1 = -180°$–$180°$ in the upper panel) and have the same scale. The orbital elements are calculated in the coordinate system with the reference plane of the initial disc.

circular disc for the eccentricities of 0.05 and 0.1, respectively. The change of the maximal radius $r_{tr,max}$ is of similar scale. The relative number of transferred particles n_{tr} changes by up to about 10 per cent for both considered disc eccentricities and is both higher and lower with respect to the circular disc. For several encounters, the change of n_{tr} is up to about ±20 per cent. In these cases however, the total number of transferred particles is small ($n_{tr} < 0.1$).

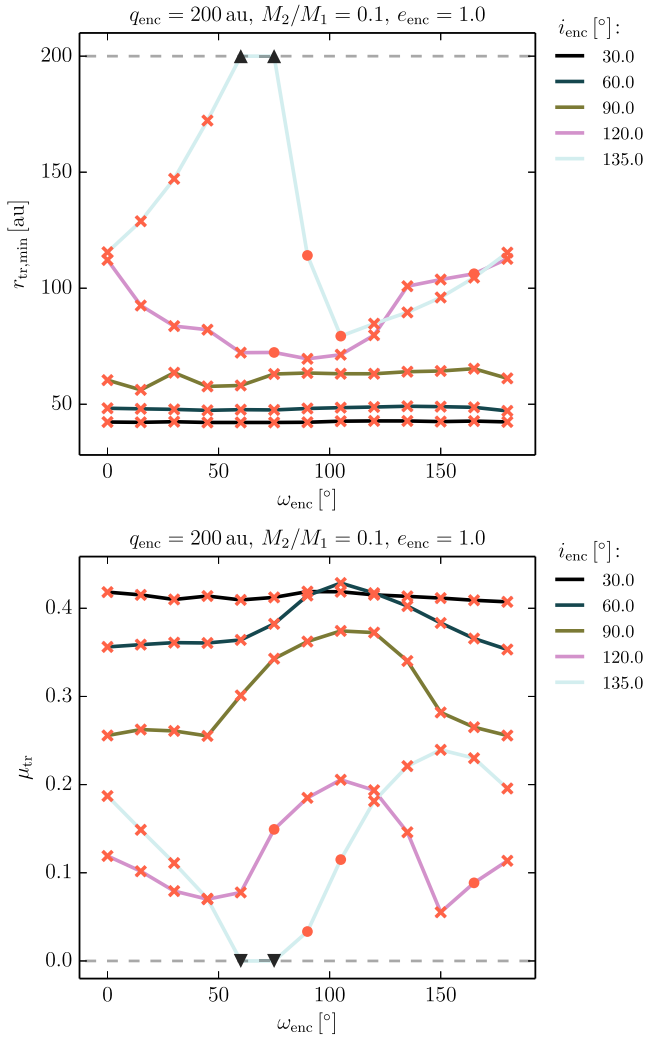

Figure 21. Minimal disc radius $r_{tr,min}$ (top) and the transfer efficiency μ_{tr} (bottom) as a function of the argument of periastron of the encounter ω_{enc}. The encounters have fixed pericentre $q_{enc} = 200$ AU, mass ratio $M_2/M_1 = 0.1$, and eccentricity $e_{enc} = 1.0$. Lines of different colour correspond to different inclinations of the encounter plane with respect to the disc i_{enc} as indicated on the right. Bullets depict the encounters with completely covered transfer region, while crosses the encounters with $r_{tr,max} > 200$ AU. Black triangles indicate the runs with $r_{tr,min} > 200$ AU and the dashed grey lines correspond to the upper and lower limit of the $r_{tr,min}$ and μ_{tr}, in the top and bottom plot, respectively.

3.7 Surface density of the planetesimal disc

As described in Section 2.2, the initial distribution of the disc particles corresponds to the surface number density $\propto 1/r$. To estimate the dependence of the transfer efficiency on the initial surface density profile, we weighted the particle counts by $1/\sqrt{r}$ to re-scale the surface density to $\propto 1/r^{1.5}$, which corresponds to the minimum mass solar nebula (Hayashi 1981). Such surface density profile changes the transfer efficiencies presented in Section 3.2 by less than 5 per cent (10 per cent) for 95 per cent (all) the coplanar encounters.

4 ANALYTIC INVESTIGATION INTO THE TRUNCATION RADIUS

In this section, we derive analytic expressions for the truncation radius for which the test particles, originally bound to star M_2, can be stripped from their parent star because of the tidal force of the passing star M_1. The truncation radius corresponds to the minimal radius of the unbound particles $r_{un,min}$ defined in Section 3.1. The stars are assumed to move in a hyperbolic orbit that is unaffected by the test particles.

4.1 Equations of motion

To describe the motion of a test particle, we use a rotating and pulsating frame (x, y, z) in which the origin corresponds to the centre of mass of the massive bodies, and in which the massive bodies are located at fixed positions along the x-axis (note that this is different from the reference frame used in our simulations that is defined in Section 2.2 and illustrated in Fig. 1). In this frame, the unit of length is varying with time, and it is given by the instantaneous relative position between the two bodies,

$$R_{12} = \frac{R_p(1+e)}{1+e\cos(\nu)} \equiv \frac{R_p(1+e)}{\lambda}. \tag{2}$$

Here, R_p, $e > 1$ and ν are the pericentre distance, eccentricity and true anomaly of the hyperbolic orbit, respectively; the range of the true anomaly is $-\arccos(-1/e) \leq \nu < \arccos(-1/e)$. For notational convenience, we define $\lambda \equiv 1 + e\cos(\nu)$. The massive bodies are located at $x = -\mu$ (body M_1) and $x = 1 - \mu$ (body M_2), where

$$\mu \equiv \frac{M_2}{M_1 + M_2}; \tag{3}$$

note that the coordinates x, y and z are in units of R_{12}. The equations of motion for the test particle in the rotating and pulsating frame are given by Duboshin (1964); for completeness, we also include a self-contained derivation in Appendix A)

$$\begin{cases} x''(\nu) - 2y'(\nu) = \frac{\partial\Omega}{\partial x}; \\ y''(\nu) + 2x'(\nu) = \frac{\partial\Omega}{\partial y}; \\ z''(\nu) + z(\nu) = \frac{\partial\Omega}{\partial z}, \end{cases} \tag{4}$$

where primes denote derivatives with respect to ν. The 'effective potential' $\Omega = \Omega(x, y, z, \nu)$ is given by

$$\Omega = \frac{1}{\lambda}\left[\frac{1}{2}\left(x^2 + y^2 + z^2\right) + \frac{1-\mu}{r_1} + \frac{\mu}{r_2}\right]. \tag{5}$$

Here r_1 and r_2 are the (scaled) distances between the test particle and the massive bodies M_1 and M_2, respectively, and are given by

$$r_1^2 = (x+\mu)^2 + y^2 + z^2; \tag{6a}$$

$$r_2^2 = (x+\mu-1)^2 + y^2 + z^2. \tag{6b}$$

For the purpose of determining the truncation radius, it is useful to apply a linear transformation to the coordinates in equation (4), such that the origin of the new coordinate system corresponds to body M_2. The new coordinates are denoted by $(\tilde{x}, \tilde{y}, \tilde{z})$, and are related to the old coordinates via

$$(\tilde{x}, \tilde{y}, \tilde{z}) = (x + \mu - 1, y, z). \tag{7}$$

The equation of motion for $\tilde{x}''(\nu)$ then reads

$$\tilde{x}'' - 2\tilde{y}' = \frac{1}{\lambda}\left[\tilde{x} + 1 - \mu - \left(\frac{1-\mu}{r_1^3}(\tilde{x}+1) + \frac{\mu}{r_2^3}\tilde{x}\right)\right]. \tag{8}$$

A useful relation between r_1 and r_2, used frequently below, is

$$r_1^2 = 1 + 2\tilde{x} + r_2^2, \tag{9}$$

which follows directly from equations (6) and (7).

4.2 Initial radial orbit around body M_2

A simple estimate can be obtained by assuming that the test particle is initially in a radial orbit around body M_2 along the $\tilde{x}$-axis, i.e. $\tilde{y} = \tilde{z} = 0$ and $y'(\nu) = 0$. For detachment from body M_2, we adopt the criterion $\tilde{x}''(\nu) = 0$ and $\tilde{x} = -r_2$ (note that $r_2 > 0$, and $\tilde{x} = r_2$ corresponds to a larger distance of the particle to body M_1, compare with equation 9). This approach is analogous to the method used to derive the Hill radius in the case that the massive bodies are in circular orbits (see for example, section 5.6 of Valtonen & Karttunen 2006). Substituting these conditions into equation (8) and using equation (9), we find

$$0 = (1 - r_2)^2 \left[\mu(1 + r_2) + r_2^2\right] |1 - r_2| - (1 - \mu) r_2^2. \tag{10}$$

Analytic solutions of equation (10) are not readily available. It is possible, however, to obtain analytic expressions for small r_2, i.e. $r_2 \ll 1$, by expanding the right-hand side of equation (10) in terms of r_2, giving the condition $\mu - (3 - 2\mu) r_2^3 \approx 0$, with (real) solution

$$r_2 \approx \left(\frac{\mu}{3 - 2\mu}\right)^{1/3}, \qquad \text{for } r_2 \ll 1. \tag{11}$$

In terms of physical units, this corresponds to a truncation radius of

$$R_t(\nu) = R_{12} r_2 \approx \frac{R_p(1 + e)}{\lambda} \left(\frac{\mu}{3 - 2\mu}\right)^{1/3}. \tag{12}$$

As expected, the truncation radius is smallest at pericentre, $\nu = 0$, in which case $\lambda = 1 + e$, and, therefore,

$$R_t(0) \approx R_p \left(\frac{\mu}{3 - 2\mu}\right)^{1/3}. \tag{13}$$

For $\mu \approx 0$, this reduces to

$$R_t(0) \approx R_p \left(\frac{\mu}{3}\right)^{1/3}, \qquad (r_2 \ll 1;\ \mu \approx 0), \tag{14}$$

which is precisely the Hill radius with the radius of the outer (circular) orbit replaced by the pericentre distance of the hyperbolic orbit. Note that $\mu \approx 0$ is assumed in the (circular) Hill problem (Valtonen & Karttunen 2006).

4.3 Initial circular orbit around body M_2 (prograde and retrograde)

A criterion that is more appropriate to the configuration studied in the numerical simulations in Sections 3.1 and 3.2, is based on the assumption that the test particles are initially in circular orbits around body M_2. The orbits do not remain circular during the encounter, but useful criteria can nevertheless be obtained with this simple assumption. We furthermore assume that the test particle orbits are coplanar with the massive bodies, that is $\tilde{z} = 0$.

The closest point in the test particle orbit to body M_1 is when the test particle intersects the $\tilde{x}$-axis, that is $\tilde{y} = 0$, and its position along the $\tilde{x}$ axis is $\tilde{x} = -r_2$. Furthermore, $\tilde{x}'(\nu) = 0$, whereas $\tilde{y}'(\nu)$ is non-zero owing to the circular motion around body M_2. In particular, using the chain rule, $\tilde{y}'(\nu)$ can be written as

$$\tilde{y}'(\nu) = \frac{\partial \tilde{y}}{\partial \nu} = \frac{\partial \tilde{y}}{\partial t}\frac{\partial t}{\partial \nu} = \frac{\partial \tilde{y}}{\partial t}\frac{1}{\dot{\nu}} = \pm\frac{\tilde{x}\omega}{\dot{\nu}}, \tag{15}$$

where $\dot{\nu}$ is given by e.g. equation (A4a), and ω is the angular frequency of the test particle around body M_2, given by

$$\omega = \sqrt{\frac{GM_2}{(R_{12} r_2)^3}} \tag{16}$$

(note that r_2 is dimensionless, and it should therefore be multiplied by R_{12} in equation 16). The positive sign in equation (15) corresponds to prograde motion of the disc test particles and the encounter of the massive bodies ($\tilde{x} < 0$, therefore $\tilde{y}' < 0$), whereas the negative sign corresponds to retrograde motion ($\tilde{y}' > 0$).

Substituting these conditions into equation (8), we find the following condition for detachment of the test particle from body M_2 (that is $\tilde{x}''(\nu) = 0$),

$$0 = \pm 2\sqrt{\mu r_2 \lambda} - \frac{(1 - r_2)^2 \left[\mu(1 + r_2) + r_2^2\right] |1 - r_2| - (1 - \mu) r_2^2}{(1 - r_2)|1 - r_2|}. \tag{17}$$

Equation (17) is not amenable to analytical solutions. Nevertheless, in the case of prograde orbits, analytic solutions can be obtained by expanding it in terms of r_2, assuming $r_2 \ll 1$. To third order in r_2,

$$\mu - 2\sqrt{r_2^3 \mu \lambda} - (3 - 2\mu) r_2^3 + \mathcal{O}\left(r_2^4\right) = 0. \tag{18}$$

Including only terms of order $r_2^{3/2}$ in equation (18), this gives

$$R_t(\nu) \approx R_p(1 + e)\left(\tfrac{\mu}{4\lambda^4}\right)^{1/3}, \tag{19a}$$

$$R_t(0) \approx R_p \left[\tfrac{\mu}{4(1+e)}\right]^{1/3}; \tag{19b}$$

also including terms of order r_2^3,

$$R_t(\nu) \approx \frac{R_p(1 + e)}{\lambda}\left[\frac{\mu}{(3 - 2\mu)^2}\right]^{1/3} \times [2\lambda + 3 - 2\mu - 2\sqrt{\lambda(\lambda + 3 - 2\mu)}]^{1/3}, \tag{20a}$$

$$R_t(0) \approx R_p \left[\frac{\mu}{(3 - 2\mu)^2}\right]^{1/3} \times [5 + 2e - 2\mu - 2\sqrt{(1 + e)(4 + e - 2\mu)}]^{1/3}. \tag{20b}$$

Unfortunately, in the case of retrograde orbits (negative sign in equation 17), we were unable to find useful analytic approximations to the solution.

In Fig. 22, we compare, for prograde orbits, the expressions in equations (19) (dashed lines) and (20) (dotted lines) to the unapproximated solution obtained by numerically solving equation (17) (solid lines). In the top panel, we show the dependence of R_t on the true anomaly; as expected, the minimum value occurs at pericentre. In the middle and bottom panels, we show the dependence on μ and e, respectively, setting $\nu = 0$. For the parameters chosen in Fig. 22 ($\mu = 0.2$ and $e = 1.5$), equation (19) gives a reasonable approximation (within a few tens of per cent) of the exact solution. equation (20) is a better approximation, differing no more than a few per cent.

In Fig. 23, we show numerical solutions of equation (17) for the cases of prograde (solid lines) and retrograde (dotted lines) orbits. In the top and bottom panels, R_t is plotted as a function of μ and e, respectively, where the fixed parameters are $\nu = 0$, $\mu = 0.2$ and $e = 1.5$. As expected, retrograde orbits are more stable, in the sense that R_t is always larger for retrograde orbits compared to prograde orbits (in Fig. 23, typically by a factor of $\sim$2). Interestingly, R_t decreases with e for prograde orbits, whereas for retrograde orbits, R_t increases with e. The dependence on e in both cases is weak, however.

The approximate solution for R_t given by equation (19) has the same dependence on μ and e as the expression for the minimal

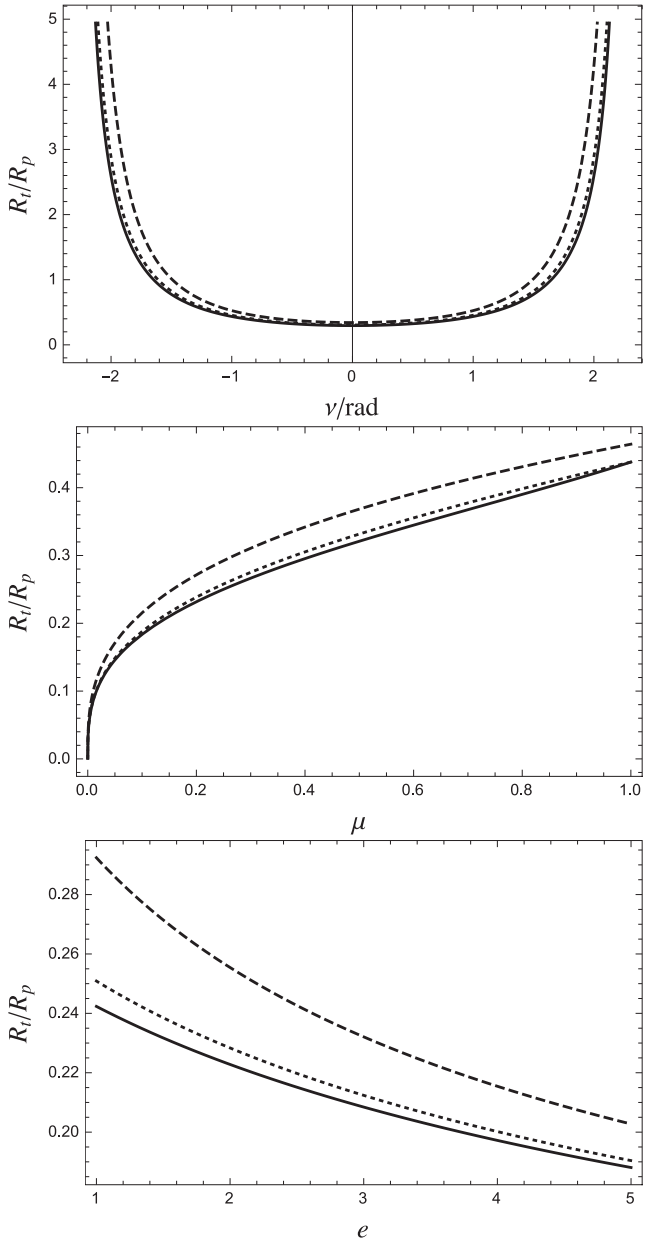

Figure 22. Truncation radius for the case of initially circular test particle orbits (cf. Section 4.3) and for prograde orbits, according to equation (19) (dashed line), equation 20) (dotted line) and equation (17) (solid line). Top panel: as a function of ν; middle panel: as a function of μ (setting $\nu = 0$); bottom panel: as a function of e (setting $\nu = 0$). Where applicable, the fixed parameters are $\mu = 0.2$ and $e = 1.5$.

radius of the unbound particles $r_{\rm un,min}$ of Kobayashi & Ida (2001, here equation 1). The two expressions differ only by a constant – Kobayashi & Ida (2001) give ≈0.34, while here we derive ≈0.63. Based on extensive simulations covering parameter space in the mass ratio and pericentre distance (larger than considered here), Breslau et al. (2014) derived an empirical formula for the truncation of the disc size after a parabolic prograde encounter, given as $0.28\,R_{\rm p}\,(M_1/M_2)^{-0.32}$. Their result has the same dependence on the encounter pericentre $R_{\rm p}$ but differs for the mass ratio – our expression (19) $\propto (M_1/M_2 + 1)^{-1/3}$. However, Breslau et al. (2014) defined the size of the disc depending on the drop in the disc radial surface density profile after the encounter and their expression might therefore not be directly comparable with our result.

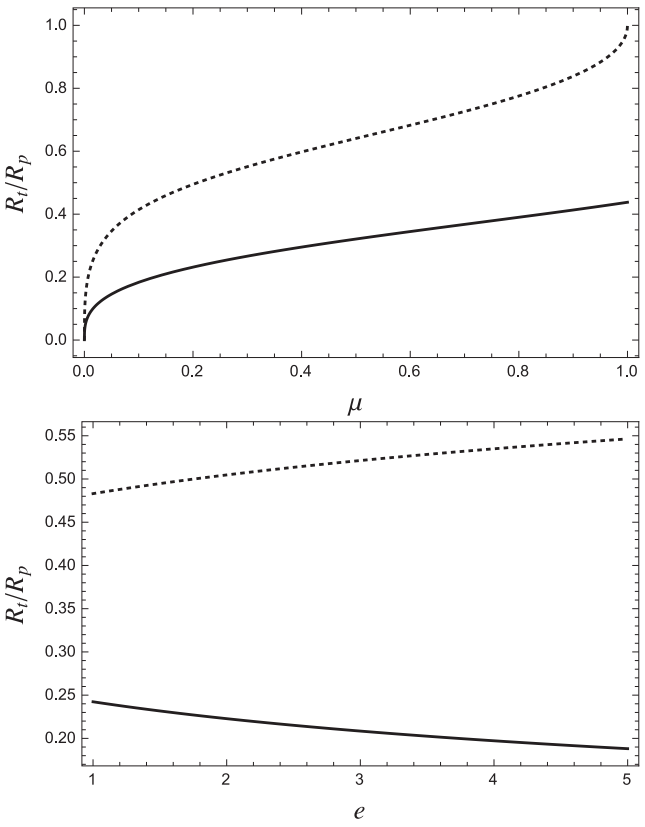

Figure 23. Truncation radius for the case of initially circular test particle orbits, for the case of prograde (solid lines) and retrograde (dotted lines) orbits, according to equation (17). In the top and bottom panels, $R_{\rm t}$ is plotted as a function of μ and e, respectively, where the fixed parameters are $\nu = 0$, $\mu = 0.2$ and $e = 1.5$.

4.4 Comparison with the simulations

The comparison of the analytic estimation of the truncation radius $R_{\rm t}$ and the minimal radius of the unbound particles derived from our simulated results $r_{\rm un,min}$ is presented in Fig. 24. We show $r_{\rm un,min}$ of the parabolic ($e_{\rm enc} = 1.0$) coplanar ($i_{\rm enc} = 0^\circ$) encounters as a function of the mass ratio M_2/M_1 and pericentre $q_{\rm enc}$. The analytic and simulated results are in a good agreement ($r_{\rm un,min}$ and $R_{\rm t}$ do not differ by more than about 11 per cent of $r_{\rm un,min}$). The bottom plot clearly shows that $r_{\rm un,min}$ is a linear function of the pericentre $q_{\rm enc}$, in agreement with equations (19) and (20). These expressions represent a good approximation to the solution of equation (17) (see Fig. 22).

As we showed in Section 3.1, the minimal radius of the unbound particles $r_{\rm un,min}$ is similar to the minimal transfer radius $r_{\rm tr,min}$ (see Fig. 7) and the expressions (17) and its approximate solutions (19) and (20) present a good estimate the minimal transfer radius for coplanar prograde encounters.

The difference between $R_{\rm t}$ and $r_{\rm un,min}$ increases for faster encounters with higher eccentricities or non-zero inclinations $i_{\rm enc}$. In the case of coplanar eccentric encounters, the analytic model describes the qualitative behaviour of $r_{\rm un,min}$ well, but tends to underestimate $r_{\rm un,min}$ by up to about 30 per cent for the most eccentric case of $e_{\rm enc} = 4.5$. We also derived analytic expressions of $R_{\rm t}$ for the

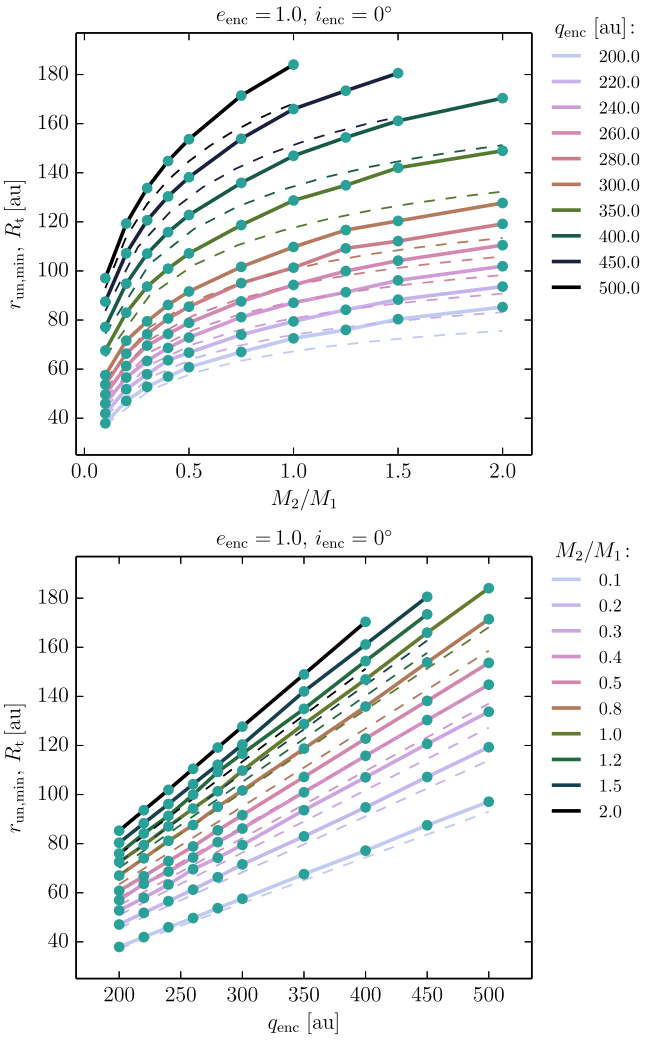

Figure 24. Comparison of the minimal radius of the particles unbound from M_2 from our simulations, $r_{un,min}$, and given by equation (17), R_t. Top panel shows $r_{un,min}$ and R_t as a function of M_2/M_1 for different q_{enc}, bottom panel then $r_{un,min}$ and R_t as a function of q_{enc} for different M_2/M_1. The dots connected by full lines indicate the simulated results, $r_{un,min}$, while the dashed lines correspond to the analytic approximation of equation (17), R_t.

inclined (non-coplanar) encounters (not given here). Their values of R_t are quantitatively in agreement with $r_{un,min}$ presented in Section 3.4 and Fig. 17, but R_t tends to underestimate $r_{un,min}$. Our analytic approach is probably too simplistic to represent the faster and inclined encounters well, for example, due to the assumption that the orbits of the test particles stay circular up to the moment when they are unbound from the parent star.

5 SUMMARY AND CONCLUSIONS

We studied the mass transfer between debris discs during close stellar encounters that are expected to often happen in star clusters and stellar associations where most stars form (Lestrade et al. 2011). We carried out simulations of an encounter of two stars on parabolic and hyperbolic orbit (eccentricity up to 4.5) where one of the stars has a debris disc represented by test particles. The mass ratio of the star initially surrounded by the disc to the one initially without was varied in the range of 0.1–2.0. The stars approached each other as close as 200–500 AU and the disc extent was fixed to 30–200 AU. We also considered the effect of the geometry of the encounter (inclination of the disc with respect to the plane of the encounter and the argument of periastron of the encounter).

The disc particles are transferred to the other star during encounters from a substantial part of the covered parameter space. We identify a restricted radial range in the initial disc, the so-called transfer region (Section 3.1), from where the particles are transferred. The limiting radii of the region depend on the parameters of the encounter. We derive an analytic description of the minimal radius from where the particles can be unbound from their parent star (Section 4) and we show how this radius compares with the minimal radius from where the particles are transferred, that is from where they end up unbound from their parent star and bound to the other star. The minimal radius of the transferred particles is typically up to 5 per cent larger than the one of the unbound particles. The analytic description of the minimal radius of the unbound particles $r_{un,min}$ can be approximated (within a few tens of per cent) as

$$r_{un,min} \approx q \left[\frac{\mu}{4(1+e)}\right]^{1/3}, \quad \text{where} \quad \mu = \frac{M_2}{M_1 + M_2},$$

and q is the pericentre of the encounter, e its eccentricity, M_1 and M_2 are the masses of the star initially without and with the disc.

The transfer efficiency – defined as the ratio of the number of transferred particles to the number of particles initially orbiting within the transfer region – depends on the encounter parameters. The efficiency is generally higher for smaller mass of the star initially with the disc, for closer approach of the two stars, and for slower encounters (that is the ones with smaller the eccentricity). As much as ∼45 per cent of the particles can be captured by the other star (Section 3.2).

The geometry of the disc and the orbit of the encounter plays an important role for the transfer region and efficiency. If the encounter orbit is inclined with respect to the disc, the minimal radius of the transfer particles is larger than for the coplanar case, and the transfer efficiency is lower. Within our resolution, the geometry with a coplanar and counter-rotating disc and encounter orbit results in no transferred particles (for the outer disc edge of 200 AU considered in our simulations), regardless of other encounter parameters. With the exception of a highly inclined retrograde orbit, the argument of pericentre of the encounter has a weaker effect. Generally, the transfer efficiency is the highest for encounters with the pericentre direction perpendicular to the intersection of the two planes, but does not change by more than 10 per cent for different values of the argument of pericentre.

The transferred particles acquire specific orbits around their new host and the population occupies a specific space of orbital elements depending on the parameters of the encounter (Fig. 20). The minimal semimajor axis of the transferred orbits is a linear function of the pericentre of the encounter, where the coefficient of the proportionality depends on the encounter eccentricity. The transferred orbits tend to be highly eccentric, with most of the encounters resulting in an eccentricity distribution with a median value of about 0.8. However, depending on the parameters of the encounter, the median eccentricity can be as low as 0.4 and particles can be transferred into almost circular orbits ($e \lesssim 0.1$). If the planes of the disc and the encounter are inclined with respect to each other, the directions of the angular momenta of more than 70 per cent of the transferred particles are restricted to a cone with a typical opening angle of less than 15°.

We find that if the disc is initially eccentric (ranges from 0.0 to 0.05 and 0.1 were considered), the transfer efficiency decreases

by no more than 10 per cent. Similarly, the initial surface density profile of the disc has a weak effect.

The eccentricities of the transferred orbits are sufficiently high ($e \gtrsim 0.05\sqrt{(a/[35\ \mathrm{AU}])}$) for the collisions between the planetesimals to be destructive and grind them into dust (Kenyon & Bromley 2002). The relative mass of the transferred planetesimals depends on the transferred region and the transfer efficiency and for the can be as high as about 40 per cent of the total initial mass of the planetesimal disc. The observability of the dust produced from the transferred planetesimals is given by further properties such as the size and temperature of the grains or their orbits and distribution around the new host star, and the estimate is beyond the scope of this work. However, we expect that the transferred material can produce an observable IR excess if its mass is at least comparable to the observed lower limits ($\gtrsim 5 \times 10^{-4}\ \mathrm{M}_{\oplus}$; Greaves et al. 2004; Wyatt 2008).

We expect that many stars could have experienced transfer among their debris discs and planetary systems. Considering the orbital characteristics of the transferred orbits, capturing planets from foreign systems presents a formation channel for objects on wide orbits of arbitrary inclinations, typically having high eccentricity but possibly also close to circular (with eccentricities about 0.1). The orbital elements of the transferred population (planetesimals or planets) can be distinct from the ones of the native objects formed around the star. This might help to identify the captured population which can be used to constrain the encounter.

ACKNOWLEDGEMENTS

We thank the anonymous referee for comments that helped to put our work better in context. We thank Susanne Pfalzner for valuable suggestions and comments on the manuscript. We thank Alan Heays, Anton Walsh and Paola Pinilla for useful discussions. We acknowledge the Leiden/ESA Astrophysics Program for Summer Students (LEAPS) for the support of MH. This work was supported by the Interuniversity Attraction Poles Programme initiated by the Belgian Science Policy Office (IAP P7/08 CHARM) and by the Netherlands Research Council NWO (grants #643.200.503, #639.073.803 and #614.061.608) and by the Netherlands Research School for Astronomy (NOVA). Part of the numerical computations were carried out using the Little Green Machine at Leiden University. We acknowledge the use of The Minor Planet Center (MPC, http://www.minorplanetcenter.net/) data base.

REFERENCES

Adams F. C., Proszkow E. M., Fatuzzo M., Myers P. C., 2006, ApJ, 641, 504
Andrews S. M., Williams J. P., 2007, ApJ, 659, 705
Baoyin H.-X., Chen Y., Li J.-F., 2010, Res. Astron. Astrophys., 10, 587
Binney J., Tremaine S., 1987, Galactic Dynamics. Princeton Univ. Press, Princeton, NJ
Bonnell I. A., Smith K. W., Davies M. B., Horne K., 2001, MNRAS, 322, 859
Breslau A., Steinhausen M., Vincke K., Pfalzner S., 2014, A&A, 565, A130
Bressert E. et al., 2010, MNRAS, 409, L54
Brown M. E., Trujillo C., Rabinowitz D., 2004, ApJ, 617, 645
Clarke C. J., Pringle J. E., 1993, MNRAS, 261, 190
Craig J., Krumholz M. R., 2013, ApJ, 769, 150
Dodson-Robinson S. E., Beichman C. A., Carpenter J. M., Bryden G., 2011, AJ, 141, 11
Dominik C., Decin G., 2003, ApJ, 598, 626
Duboshin G. N., 1964, Nebesnaya mekhanika. Analiticheskie i kachestvennye metody (Celestial Mechanics. Analytical and Quality Methods). Nauka, Moscow
Eiroa C. et al., 2013, A&A, 555, A11
Fujii M., Iwasawa M., Funato Y., Makino J., 2007, PASJ, 59, 1095
Gieles M., Portegies Zwart S. F., 2011, MNRAS, 410, L6
Gonçalves Ferrari G., Boekholt T., Portegies Zwart S. F., 2014, MNRAS, 440, 719
Greaves J. S., Wyatt M. C., Holland W. S., Dent W. R. F., 2004, MNRAS, 351, L54
Hall S. M., Clarke C. J., Pringle J. E., 1996, MNRAS, 278, 303
Hayashi C., 1981, Prog. Theor. Phys. Suppl., 70, 35
Hurley J. R., Shara M. M., 2002, ApJ, 565, 1251
Jílková L., Portegies Zwart S., 2015, MNRAS, 451, 804
Jílková L., Portegies Zwart S., Pijloo T., Hammer M., 2015, MNRAS, 453, 3157
Kennedy G. M., Wyatt M. C., 2010, MNRAS, 405, 1253
Kenyon S. J., Bromley B. C., 2002, AJ, 123, 1757
Kenyon S. J., Bromley B. C., 2004a, AJ, 127, 513
Kenyon S. J., Bromley B. C., 2004b, Nature, 432, 598
Kenyon S. J., Bromley B. C., 2008, ApJS, 179, 451
Kobayashi H., Ida S., 2001, Icarus, 153, 416
Kobayashi H., Ida S., Tanaka H., 2005, Icarus, 177, 246
Krivov A. V., 2010, Res. Astron. Astrophys., 10, 383
Lada C. J., Lada E. A., 2003, ARA&A, 41, 57
Larwood J. D., Kalas P. G., 2001, MNRAS, 323, 402
Lestrade J.-F., Morey E., Lassus A., Phou N., 2011, A&A, 532, A120
Levison H. F., Duncan M. J., Brasser R., Kaufmann D. E., 2010, Science, 329, 187
Luk'yanov L. G., 2010, Astron. Lett., 36, 823
Malmberg D., de Angeli F., Davies M. B., Church R. P., Mackey D., Wilkinson M. I., 2007, MNRAS, 378, 1207
Matthews B. C., Krivov A. V., Wyatt M. C., Bryden G., Eiroa C., 2014, in Beuther H., Klessen R. S., Dullemond C. P., Henning T., eds, Protostars and Planets VI. Univ. Arizona Press, Tucson, AZ, p. 521
Melita M. D., Larwood J. D., Williams I. P., 2005, Icarus, 173, 559
Morbidelli A., Levison H. F., 2004, AJ, 128, 2564
Muñoz D. J., Kratter K., Vogelsberger M., Hernquist L., Springel V., 2015, MNRAS, 446, 2010
Mustill A. J., Wyatt M. C., 2009, MNRAS, 399, 1403
Olczak C., Pfalzner S., Spurzem R., 2006, ApJ, 642, 1140
Olczak C., Pfalzner S., Eckart A., 2008, A&A, 488, 191
Olczak C., Pfalzner S., Eckart A., 2010, A&A, 509, A63
Olczak C., Kaczmarek T., Harfst S., Pfalzner S., Portegies Zwart S., 2012, ApJ, 756, 123
Ostriker E. C., 1994, ApJ, 424, 292
Parker R. J., Quanz S. P., 2012, MNRAS, 419, 2448
Pelupessy F. I., Portegies Zwart S., 2013, MNRAS, 429, 895
Pelupessy F. I., Jänes J., Portegies Zwart S., 2012, New Astron., 17, 711
Pelupessy F. I., van Elteren A., de Vries N., McMillan S. L. W., Drost N., Portegies Zwart S. F., 2013, A&A, 557, A84
Pfalzner S., 2003, ApJ, 592, 986
Pfalzner S., Vogel P., Scharwächter J., Olczak C., 2005a, A&A, 437, 967
Pfalzner S., Umbreit S., Henning T., 2005b, ApJ, 629, 526
Pfalzner S., Olczak C., Eckart A., 2006, A&A, 454, 811
Portegies Zwart S., 2016, MNRAS, 457, 313
Portegies Zwart S. F., Jílková L., 2015, MNRAS, 451, 144
Portegies Zwart S. F., McMillan S. L. W., van Elteren A., Pelupessy F. I., de Vries N., 2013, Comput. Phys. Communications, 184, 456
Punzo D., Capuzzo-Dolcetta R., Portegies Zwart S., 2014, MNRAS, 444, 2808
Reche R., Beust H., Augereau J.-C., 2009, A&A, 493, 661
Rosotti G. P., Dale J. E., de Juan Ovelar M., Hubber D. A., Kruijssen J. M. D., Ercolano B., Walch S., 2014, MNRAS, 441, 2094
Spurzem R., Giersz M., Heggie D. C., Lin D. N. C., 2009, ApJ, 697, 458
Steinhausen M., Olczak C., Pfalzner S., 2012, A&A, 538, A10

Su K. Y. L. et al., 2006, ApJ, 653, 675
Thureau N. D. et al., 2014, MNRAS, 445, 2558
Toomre A., Toomre J., 1972, ApJ, 178, 623
Trujillo C. A., Sheppard S. S., 2014, Nature, 507, 471
Valtonen M., Karttunen H., 2006, The Three-Body Problem. Cambridge Univ. Press, Cambridge
Vincke K., Breslau A., Pfalzner S., 2015, A&A, 577, A115
Wyatt M. C., 2008, ARA&A, 46, 339
Wyatt M. C., Dent W. R. F., 2002, MNRAS, 334, 589
Zheng X., Kouwenhoven M. B. N., Wang L., 2015, MNRAS, 453, 2759

APPENDIX A: DERIVATION OF THE EQUATIONS OF MOTION IN A ROTATING AND PULSATING FRAME FOR THE HYPERBOLIC RESTRICTED THREE-BODY PROBLEM

Here, we give a self-contained derivation of the equations of motion in a rotating and pulsating frame for the hyperbolic restricted three-body problem, which we used in Section 4. Similar equations have been given by Duboshin (1964) and Luk'yanov (2010). Our derivation is an extension of the derivation presented in Baoyin, Chen & Li (2010), where the equations of motion were derived for the elliptic restricted three-body problem.

We assume that two massive bodies, bodies 1 and 2, are in a hyperbolic orbit, with separation R_{12} given by equation (2). Their position vectors with respect to an inertial frame are denoted by $\boldsymbol{R}_i = \{X_i, Y_i, Z_i\}$, with $i \in \{1, 2\}$. Without loss of generality, the orbital plane of the massive bodies is set to coincide with the XY plane, i.e. $Z_1 = Z_2 = 0$. The Newtonian equations of motion for the test particle, with position vector $\boldsymbol{R} = \{X, Y, Z\}$, are given by

$$\frac{\mathrm{d}^2\boldsymbol{R}}{\mathrm{d}t^2} = -GM_1\frac{\boldsymbol{R}-\boldsymbol{R}_1}{||\boldsymbol{R}-\boldsymbol{R}_1||^3} - GM_2\frac{\boldsymbol{R}-\boldsymbol{R}_2}{||\boldsymbol{R}-\boldsymbol{R}_2||^3}. \tag{A1}$$

Next, we define a rotating and pulsating frame $\boldsymbol{r} = (x, y, z)$ in which the massive bodies are at fixed positions along the x-axis, $x_1 = -\mu$ and $x_2 = 1-\mu$, where μ is defined in equation (3), and the unit of length is the instantaneous separation $R_{12} = R_{12}(\nu)$. The relation between the dimensionless vector $\boldsymbol{r}$ in the new frame, and the dimensional vector $\boldsymbol{R}$ in the old frame, is given by

$$\boldsymbol{R} = R_{12}\mathbf{M}\cdot\boldsymbol{r}, \qquad \mathbf{M} = \begin{pmatrix} \cos(\nu) & -\sin(\nu) & 0 \\ \sin(\nu) & \cos(\nu) & 0 \\ 0 & 0 & 1 \end{pmatrix}. \tag{A2}$$

Our procedure is to express both sides of equation (A1) in terms of quantities pertaining only to the new frame and with the time transformed to the true anomaly ν. This yields a set of second-order differential equations for $\boldsymbol{r}''(\nu)$, i.e. equations (4).

First, we consider the left-hand side equation (A1). By applying the chain rule, the inertial acceleration can be written as

$$\frac{\mathrm{d}^2\boldsymbol{R}}{\mathrm{d}t^2} = \dot{\nu}^2\frac{\mathrm{d}\boldsymbol{R}}{\mathrm{d}\nu^2} + \ddot{\nu}\frac{\mathrm{d}\boldsymbol{R}}{\mathrm{d}\nu}. \tag{A3}$$

For hyperbolic orbits, $\dot{\nu}$ and $\ddot{\nu}$ are given by

$$\dot{\nu} = \sqrt{\frac{G(M_1+M_2)}{R_\mathrm{p}^3}}\frac{\lambda^2}{(1+e)^{3/2}}; \tag{A4a}$$

$$\ddot{\nu} = -\frac{G(M_1+M_2)}{R_\mathrm{p}^3}\frac{2e\lambda^3\sin(\nu)}{(1+e)^3}, \tag{A4b}$$

where $\lambda \equiv 1 + e\cos(\nu)$. Applying equation (A2) to equation (A3) and substituting equations (A4), we find

$$\frac{\mathrm{d}^2X}{\mathrm{d}t^2} = -\alpha\{\cos(\nu)x(\nu) - \sin(\nu)y(\nu) + \lambda\cos(\nu)[2y'(\nu) - x''(\nu)] + \lambda\sin(\nu)[2x'(\nu) + y''(\nu)]\}; \tag{A5a}$$

$$\frac{\mathrm{d}^2Y}{\mathrm{d}t^2} = -\alpha\{\sin(\nu)x(\nu) + \cos(\nu)y(\nu) + \lambda\sin(\nu)[2y'(\nu) - x''(\nu)] - \lambda\cos(\nu)[2x'(\nu) + y''(\nu)]\}; \tag{A5b}$$

$$\frac{\mathrm{d}^2Z}{\mathrm{d}t^2} = \alpha\left\{\lambda z''(\nu) + (\lambda-1)z(\nu)\right\}, \tag{A5c}$$

where

$$\alpha \equiv \frac{G(M_1+M_2)}{R_\mathrm{p}^2}\frac{\lambda^2}{(1+e)^2}. \tag{A6}$$

Next, we consider the right-hand side of equation (A1). By applying equation (A2) to $||\boldsymbol{R}-\boldsymbol{R}_i||^2 = (X-X_i)^2 + (Y-Y_i)^2 + Z^2$, the latter can be written as

$$||\boldsymbol{R}-\boldsymbol{R}_1||^2 = R_{12}^2\left[(x+\mu)^2 + y^2 + z^2\right] \equiv R_{12}^2 r_1^2; \tag{A7a}$$

$$||\boldsymbol{R}-\boldsymbol{R}_2||^2 = R_{12}^2\left[(x+\mu-1)^2 + y^2 + z^2\right] \equiv R_{12}r_2^2, \tag{A7b}$$

where we introduced the dimensionless distances r_1 and r_2 (cf. equation 6). Also applying equation (A2) to the terms $\boldsymbol{R}-\boldsymbol{R}_i$ in equation (A1), the components A_X, A_Y and A_Z of the right hand of equation (A1), i.e. the inertial gravitational acceleration, can be written as

$$A_X = -\alpha\left\{\cos(\nu)\mu(1-\mu)\left(\frac{1}{r_1^3} - \frac{1}{r_2^3}\right) + \left(\frac{1-\mu}{r_1^3} + \frac{\mu}{r_2^3}\right)[\cos(\nu)x(\nu) - \sin(\nu)y(\nu)]\right\}; \tag{A8a}$$

$$A_Y = -\alpha\left\{\sin(\nu)\mu(1-\mu)\left(\frac{1}{r_1^3} - \frac{1}{r_2^3}\right) + \left(\frac{1-\mu}{r_1^3} + \frac{\mu}{r_2^3}\right)[\sin(\nu)x(\nu) + \cos(\nu)y(\nu)]\right\}; \tag{A8b}$$

$$A_Z = -\alpha\left(\frac{1-\mu}{r_1^3} + \frac{\mu}{r_2^3}\right)z(\nu). \tag{A8c}$$

Equating the three components in equations (A5) and (A8) and solving for $\{x''(\nu), y''(\nu), z''(\nu)\}$, we find the equations of motion given by equations (4).

This paper has been typeset from a TEX/LATEX file prepared by the author.